Bulletin of the Seismological Society of America, Vol. 101, No. 2, pp. 826–847, April 2011, doi: 10.1785/0120090232

Using the SPAC Microtremor Method to Identify 2D Effects and Evaluate 1D Shear-Wave Velocity Profile in Valleys

by M. Claprood, M. W. Asten, and J. Kristek

Abstract The requirement of a layered-earth geology is a restrictive assumption when using the spatially averaged coherency spectra (SPAC) method. Numerical simulations of microtremors and SPAC observations recorded in the Tamar paleovalley, Launceston (Tasmania, Australia), are used to assess the potential of the SPAC method to identify two-dimensional (2D) effects and evaluate one-dimensional (1D) shear-wave velocity (SWV) profile in a valley environment. The Tamar Valley is approximately 250 m deep by 700–1000 m wide. It is filled with soft sediments from the Tertiary and Quaternary periods above hard dolerite bedrock of Jurassic age.

Observed coherency spectra of the vertical component are analyzed at two sites in the Tamar Valley; using two 50-m-radius centered triangular arrays above the deepest point of the valley at site DBL, and above the east flank of the valley at site RGB. Simulated and observed coherency spectra suggest the propagation of Rayleigh waves of first higher mode at the *SV* frequency of resonance of the Tamar Valley affects the coherency spectra recorded with pairs of sensors perpendicular to the valley (transverse-COH). Simulated and observed coherency spectra recorded above the deepest point of the valley (site DBL) with pairs of sensors parallel to the valley axis (axial-COH) are not affected by these edge-generated Rayleigh waves and agree well with the theoretical coherency spectrum computed from the preferred 1D SWV profile.

The simulated and observed results from this paper suggest that differences between the observed axial-COH and transverse-COH give an indication of the existence of the 2D buried valley. Results also suggest that the observed coherency spectra recorded on pairs of sensors oriented parallel to the valley axis can provide a reliable evaluation of a 1D SWV profile above the deepest point of a deep and narrow valley, such as the Tamar Valley.

Introduction

Microtremor survey methods to evaluate the shear-wave velocity (SWV) profile at specific sites, using the constant ambient vibrations of the ground (referred to as microtremors) generated by human activities (at frequency $f \geq 1$ Hz) or natural phenomena (at $f \leq 1$ Hz) as the source of energy (Okada, 2003) are gaining in popularity. The microtremor survey methods are ideally suited for urban environment; they are noninvasive, and their source of energy is continuous in proximity to urban agglomerations. An important proportion of microtremor energy is associated with the propagation of surface waves (Aki, 1957; Capon, 1969; Horike, 1985; Tokimatsu, 1997; Okada, 2003; Bonnefoy-Claudet *et al.*, 2006), with fundamental mode Rayleigh waves dominating. The dominance of fundamental mode Rayleigh waves is a function of several factors, such as the complexity of SWV structure (Tokimatsu *et al.*, 1992). This hypothesis is important when dealing with the vertical component of microtremors, which, in the absence of anisotropy, are only present in Rayleigh surface waves (Udías, 1999).

Different processing techniques have been developed to evaluate SWV structures from the frequency dispersive velocity curves of microtremor propagation. The most common array-based microtremor methods are the spatial autocorrelation method developed by Aki (1957), also termed the spatially averaged coherency spectra (SPAC) method (Asten, 2006a); the frequency–wavenumber (FK) method introduced by Toksöz and Lacoss (1968), with two processing algorithms developed by Lacoss *et al.* (1969) and Capon (1969); and the multiple signal classification (MUSIC) method presented by Schmidt (1986) and Goldstein and Archuleta (1987). Alternative SPAC processing include the centerless circular array method introduced by Cho *et al.* (2004, 2006, 2008) and the single circular array method introduced by García-Jerez *et al.* (2008). By recording synthetic ambient noise with a dense array of sensors, Wathelet

et al. (2008) concluded there is no significant difference in the evaluation of SWV profile with the FK or SPAC method.

The microtremor survey methods require the hypothesis of temporal and spatial stationarity of the microtremor wave field, so it can be treated as a stochastic process (Aki, 1957). This hypothesis is generally valid when recording long (but still less than 1 hr) microtremor time series, using an array with an aperture smaller than one or two kilometers (Toksöz, 1964). The temporal and spatial stationarity of microtremors is essential to validate because unstationarity on the power spectra makes them time-dependent and impossible to treat as a simple function of frequency (Toksöz, 1964). By recording microtremors over a long period of time with an array of sensors, microtremors can be analyzed as an assemblage of coherent waves traveling in various directions and covering an extended interval of frequencies.

An important hypothesis to consider when using array-based microtremor survey methods is that all sensors of the array must sample the same geology. This hypothesis restricts the use of microtremor survey methods to regions where the geology can be approximated by a layered earth. This requirement is very restrictive in the evaluation of SWV at specific sites, and several authors have evaluated the use of the microtremor survey methods above more complex geology. For example, several studies used single-station microtremor observations, such as the standard spectral ratio (SSR) and horizontal-to-vertical spectrum ratio (HVSR), to identify the modes and frequencies of resonance that develop in valleys (Field, 1996; Steimen *et al.*, 2003; Uebayashi, 2003; Roten *et al.*, 2006). While some authors have used HVSR observations to evaluate SWV profiles (Arai and Tokimatsu, 2004), Asten *et al.* (2002) and Chávez-García *et al.* (2007) demonstrated that single-station microtremor observations show poor resolution in evaluating SWV profile and most often require *a priori* knowledge of the velocity structure for site resonance study in valley environments.

Some authors have developed methodologies to use array-based microtremor observations in complex geology. Cornou *et al.* (2003a, 2003b) used the MUSIC algorithm with HVSR observations to identify the wave field associated with site amplification in the Grenoble Valley (France), using an extensive array of 29 three-component seismometers and a total array aperture of 1 km. Hartzell *et al.* (2003) used the FK and MUSIC methods to detect edge-generated surface waves with a dense array of 52 sensors in the Santa Clara Valley (U.S.A.), using site response spectra from earthquake-generated motion to evaluate the SWV profile. Roten *et al.* (2006) and Roten *et al.* (2008) used the FK method to identify the expected modes of resonance in the Rhône Valley (Switzerland); and Roten and Fäh (2007) evaluated the SWV profile in the Rhône Valley, using a joint inversion on the velocity dispersion curve obtained with the FK method and two-dimensional (2D) resonance frequencies observed on an SSR profile. Recently, Picozzi *et al.* (2009) used high-frequency seismic noise tomography to image shallow structural heterogeneities with an array of 21 geophones at the Nauen test site in Germany.

The SPAC method requires a broad azimuthal distribution of energy sources to achieve best results (Asten, 2003, 2006a). This particularity is of interest when recording ambient seismic noise in a urban environment because cities provide microtremor sources from various and unknown origins. The FK method is more reliable when a preferential source of microtremor energy is identified. The need for a wide azimuthal source distribution is an important requirement in order to obtain reliable results with the SPAC method. Results obtained by Cho *et al.* (2004, 2006a) and Asten (2003, 2006a) showed a departure between the observed and theoretical coherency spectra with limited source azimuth sampling. This outlines the importance of verifying the source distribution of the microtremor wave field in the SPAC method flowchart (Aki, 1957).

The SPAC method requires fewer sensors than the FK method to achieve similar resolution (Henstridge, 1979; Kudo *et al.*, 2002; Chávez-García *et al.*, 2005; Okada, 2006), reducing human labor and equipment and simplifying the logistics of field data acquisition. It also offers better resolution at low frequency (corresponding to deep material) for the same array size (Asten, 1976; Okada, 2003; Hartzell *et al.*, 2005; Claprood and Asten, 2009a), which justifies the deployment of smaller arrays to achieve good resolution at depth. Because SPAC arrays are constrained to regular array geometry (which can be difficult to achieve in an urban environment), the smaller dimensions of the array and the use of fewer sensors for the SPAC method are advantageous when deploying the equipment in a city.

The approximation of a layered-earth geology is an important restriction when using the SPAC method. To the best of our knowledge, little work has been done to analyze the capabilities of the SPAC method in 2D environments. This paper presents an alternative approach to the FK method in 2D environments, profiting from the recognized advantages of the SPAC method (fewer sensors and smaller array geometry) and quantifying perturbations on SPAC data induced by departures from the usual assumption of layered geology. The objectives are (1) to recognize such perturbations by optimizing the direction between sensors and (2) to analyze the potential of SPAC observations to evaluate one-dimensional 1D SWV profiles in 2D environments. Microtremor observations were recorded in the city of Launceston (Tasmania, Australia), where the presence of the Tertiary-age Tamar Valley has been outlined, in-filled with soft sediments that vary rapidly in thickness from 0 m to 250 m over a few hundreds of meters.

Geophysical Settings

Information on the geology of Launceston is available from unpublished maps from Mineral Resources Tasmania, borehole logs held by Launceston City Council, and a gravity survey completed by Leaman (1994). The geological map of

Launceston presented in Figure 1 outlines the rapid changes in surface geology in the central business district of Launceston, with the geological interpretation of two gravity profiles recorded across the valley.

The bedrock at Launceston comprises dense, fractured, and weathered Jurassic dolerite (Fig. 1a, zone a), which provides reduced seismic risk and excellent foundation conditions (Leaman, 1994). It is covered by poorly consolidated materials (i.e., clays, sands, conglomerates, silts, and fills), which can be compressible, water saturated, plastic, and of low density. Quaternary alluvial sediments (silts, gravels, fills) were deposited in the valley floor and other marshy areas near sea level (Fig. 1a, zones d and e). These sediments have poor cohesion and negligible strength, and they may be thixotropic. Low density Tertiary sands and clays fill the ancient valley systems beneath Launceston (Fig. 1a, zones f). The gravity interpretation of Leaman (1994) identified two paleovalley systems in Launceston: the Tamar paleovalley and the North Esk paleovalley, both trending in a north–northwest to south–southeast direction. Interpretation of the gravity survey indicates that the Tamar Valley has a width of 700–1000 m and a maximum depth of approximately 250 m (Fig. 1b). The Tamar Valley is the focus of our research because it is more continuous and better defined than the North Esk Valley.

SPAC Microtremor Method

Microtremors are recorded with an array of geophones to evaluate the coherency spectrum between all pairs of sensors in the array. Spatially averaged coherency spectra are then computed for multiple interstation separations by azimuthal averaging. When recording microtremors from all sources and directions with an array of n sensors azimuthally distributed at distance r from a center sensor, the complex coherency spectrum $C_{jc}(f)$ evaluated by each pair of sensors is computed as:

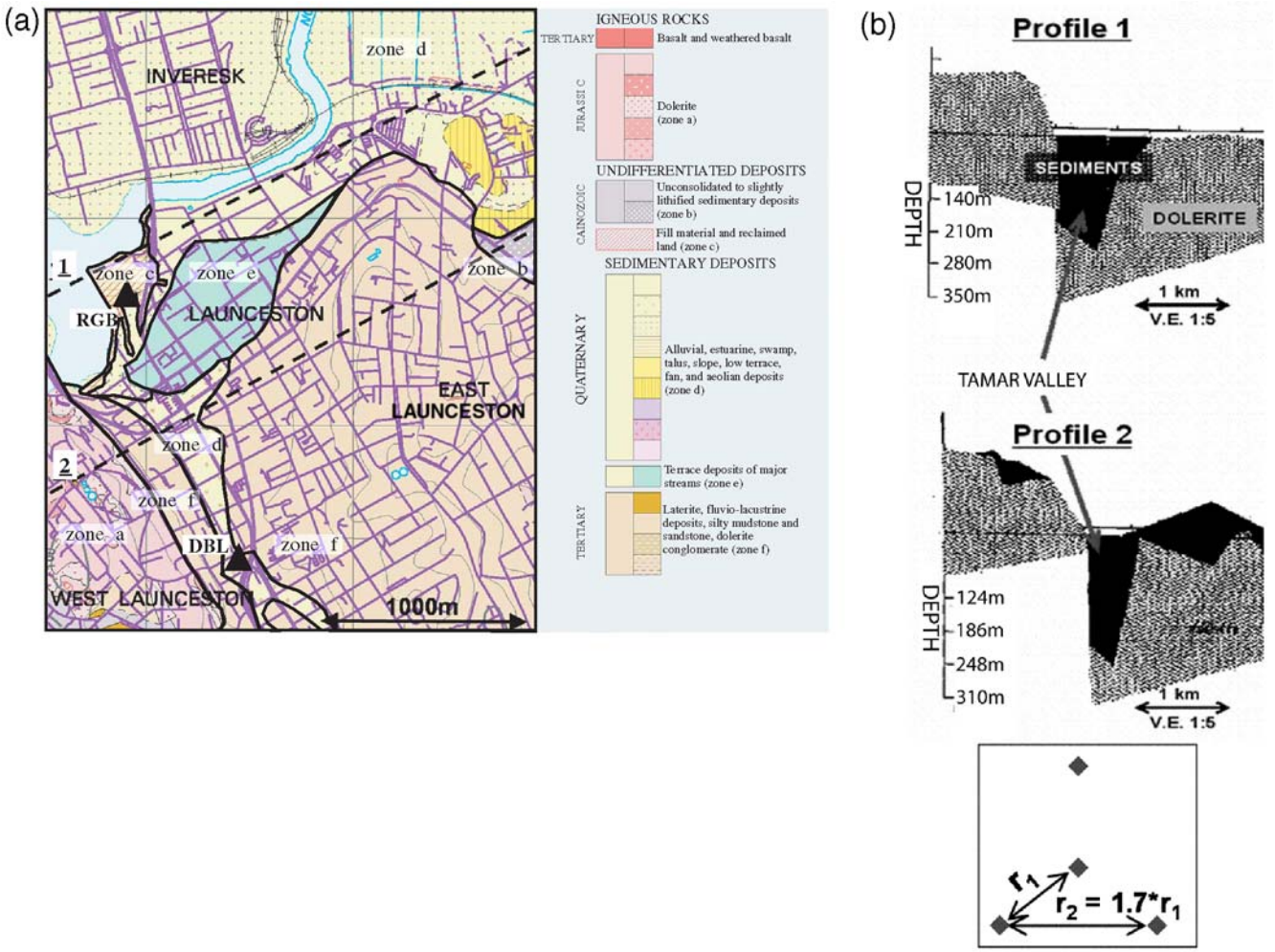

Figure 1. (a) Map of surface geology of Launceston (modified from Mineral Resources Tasmania). The map is divided into six zones delimited by thick black lines. Triangles are the location of SPAC microtremor observations at sites DBL and RGB. Dashed lines indicate the location of two gravity profiles from Leaman (1994), presented in panel (b). The bottom of (b) shows the centered triangular SPAC array geometry with interstation separations r_1 and r_2. The color version of this figure is available only in the electronic edition.

$$C_{jc}(f) = \exp\{ikr_{jc}\cos(\theta_{jc} - \phi)\}, \quad (1)$$

where i is the imaginary unit number; k is the spatial wavenumber at frequency f; r_{jc} is the interstation separation of the jth sensor relative to the center sensor c, with azimuth θ_{jc}; and ϕ is the propagation azimuth of a single plane wave across the array (Asten, 2006a). When considering an infinite number of sensors positioned around a center sensor, the integration of coherencies $C_{jc}(f)$ with azimuth leads to the spatially averaged coherency spectrum $C(f)$ (Aki, 1957; Okada, 2003):

$$C(f) = \frac{1}{2\pi}\int_0^{2\pi} \exp\{ikr\cos(\theta - \phi)\}d\theta, \quad (2)$$

which can be expressed as the Bessel function of the first kind and zero order J_0 of variable rk:

$$C(f) = J_0(kr) = J_0\left(\frac{2\pi f r}{V(f)}\right), \quad (3)$$

where $V(f)$ is the surface wave velocity dispersion function of a layered-earth model for which the 1D SWV profile is evaluated.

Aki (1957) demonstrated the possibility of using the horizontal components of a microtremor wave field to resolve for the Rayleigh and Love wave dispersion curves, gaining constraints on the SWV profile. Köhler *et al.* (2007) and Fäh *et al.* (2007) presented the advantages of the additional information gained about Love waves when using the three-component SPAC and FK methods, respectively. For its simpler processing, the traditional SPAC method (using the vertical component only) is used in this paper.

Modifications to the conventional SPAC processing have been developed to permit its use with arrays that deviate from the standard circular and equidistant configuration (Bettig *et al.*, 2001; Ohori *et al.*, 2002; Cho *et al.*, 2004; Köhler *et al.*, 2007). This idea was originally proposed by Aki (1957) and mathematically demonstrated by Capon (1973), who proved that identical results are obtained when using either a single pair of sensors to record an omnidirectional wave field or an array of n sensors to record one single plane wave of unique azimuth. The integration of complex coherency spectra is adapted to sum over the sources azimuth ϕ, with the sensors orientation θ fixed.

Some authors proposed using a single pair of sensors to evaluate the coherency spectrum, replacing the spatial averaging by temporal averaging and increasing the length of the microtremor time series (Aki, 1957; Morikawa *et al.*, 2004; Chávez-García *et al.*, 2005). By increasing the recording time, the probability to respect the azimuthal distribution of microtremor sources increases considerably, which improves the reliability of SPAC observations recorded with a pair of sensors. Following the recommendations from Okada (2006) and Claprood and Asten (2010), we restrict the analysis to frequencies up to the first minimum of the Bessel function when using a single pair of sensors.

The domain of validity of the frequency interval to interpret SPAC observations with an array of sensors is still debated in the literature. Henstridge (1979) first proposed to restrict the valid frequency interval to $0.4 \leq rk \leq 3.2$, where rk is the argument of the Bessel function (r is the interstation separation, k is the wavenumber). The upper limit corresponds to the Nyquist frequency, which limits the interpretation at high frequency. Okada (2006) further investigated that upper limit, suggesting it is restricted by the number of sensors in the array and approximately corresponds to the first minimum of the theoretical Bessel function. Asten (2006a, 2006b) suggested that the multiple mode SPAC method (MMSPAC) can be reliable to frequencies as high as $rk \simeq 20$ when the microtremor wave field has adequate azimuthal coverage and that the upper frequency should be determined by analyzing the microtremor wave field. The upper frequency limit was pushed to extreme limits by Ekström *et al.* (2009). We followed the MMSPAC philosophy in this study when using the spatially averaged coherency spectra, selecting the interval of valid frequencies on a case-by-case scenario. The valid frequency range is identified on each selected site on the coherency spectra.

Field Procedure

Microtremor observations were recorded in October 2007 in the city center of Launceston, using four three-component Guralp CMG-3ESP 30-s and 60-s period geophones. Coherency spectra are observed at two separate sites, DBL and RGB, located within the assumed limits of the Tamar Valley (Fig. 1a). SPAC observations were recorded with time series of 20–30 minutes, sufficient to ensure reliability in the observed coherency spectra computed with a limited number of sensors (Chávez-García and Rogríguez, 2007; Chávez-García *et al.*, 2007; Claprood and Asten, 2010). The time series are divided into time segments of 80 seconds with 50% overlap, which are weighted with a Hanning bell and then fast-Fourier transformed in the frequency domain to obtain the raw spectra $S_i(f)$ of microtremor energy at every sensor i. The coherency spectrum between each pair of sensors (i, j) is computed using the equation:

$$C_{ij}(f) = \frac{S_i(f)S_j^*(f)}{\sqrt{S_i(f)S_i^*(f)S_j(f)S_j^*(f)}}, \quad (4)$$

where $C_{ij}(f)$ is the complex coherency and * denotes the complex conjugate. Complex coherency spectra are averaged over all time segments to yield the temporally averaged coherency spectrum at each pair of sensors.

Spatially averaged coherency spectra are computed by averaging over azimuth for interstation separations r_1 and r_2, available from the centered triangular arrays used in Launceston (Fig. 1b, bottom). The MMSPAC method is followed

to interpret SPAC observations because of its increased precision in the evaluation of SWV profiles. The MMSPAC method also helps at the recognition of higher modes of propagation and justifies the use of fewer sensors and arrays of smaller dimensions. Asten (2005), Roberts and Asten (2005), and Stephenson *et al.* (2009) presented case studies in which the advantages of the MMSPAC method are outlined.

The real component of observed coherency spectra is directly fit to the theoretical coherency spectrum J_0 by least-square optimization of successive forward modeling (Herrmann, 2002) to evaluate the SWV profiles without evaluating the surface wave velocity dispersion function. Asten *et al.* (2004) indicated that the direct fit of coherency spectra ensures minimal loss of information when evaluating the SWV profile. Assuming the predominance of the fundamental mode of propagation of Rayleigh-type surface wave, the fit between the observed and inverted theoretical coherency spectra is quantified by minimizing the mean square of residuals (MSR). The MSR is obtained by dividing the sum of the square of residuals (SSR) between observed and theoretical coherency spectra by the length of the frequency vector.

The MSR is used as an alternative to the SSR traditionally employed to compare observations to theoretical models. The MSR was found to be the preferred option to compare observed coherency spectra computed on different frequency intervals (Claprood and Asten, 2010). The MSR is insensitive to the length of the frequency interval while the SSR varies proportionally with the length of the frequency support. When comparing two vectors of the same length, results analyzed with the MSR are equivalent to results analyzed with the SSR. A sensitivity study was completed to analyze the precision and uniqueness of the preferred SWV profile evaluated.

Asten (2006a) suggested analyzing the behavior of the imaginary component of the coherency spectrum by separating it into a smoothed and roughened components. Any cyclic behavior of the smoothed imaginary component gives indication about the distribution of the microtremor wave field; while the root mean square of the roughened imaginary component $\mathrm{rms}_{\mathrm{Im}}$ is an evaluation of statistical noise on the microtremor observations.

We propose the hypothesis that the presence of the Tamar Valley impacts the observed coherency spectrum differently, depending on the orientation of the pair of sensors from which it is computed. Coherency spectra recorded by pairs of sensors oriented axially and transverse to the valley axis are likely to present the most significant differences. This will affect the reliability of the SWV profile if traditionally computed from the spatially averaged coherency spectrum. By analyzing the coherency spectra observed from each pair of sensors of varying azimuth (Claprood and Asten, 2010), we study the spatial distribution of the microtremor wave field and the valid range of frequencies at sites DBL and RGB. The MSR computed between the observed coherency spectrum on each pair of sensors and the theoretical coherency spectrum is used to quantitatively assess the resolution of the coherency spectra recorded by pairs of sensors of different azimuth. It is an alternative to the FK method to evaluate the azimuth distribution of the microtremor wave field when using a limited number of sensors to record microtremors.

Having access to only four low-frequency seismometers, coherency spectra were successively recorded with two centered triangular arrays of different orientations to form a nonuniform hexagonal array at each site. The first array was oriented with the pair of sensors XA_1 (X is the center sensor, A_1 is the first sensor on the array circumference) parallel to the axis of the Tamar Valley (azimuth $\theta_1 = 135°$ or 315° relative to geographic true north). The second array is oriented with the pair of sensors XA_2 transverse to the valley axis (azimuth $\theta_2 = 45°$ or 225°). The orientation of each array is shown in Figure 2. We use the term "axial-COH" to designate the coherency spectrum recorded with a pair of sensors oriented parallel to the valley axis and "transverse-COH" for the coherency spectrum recorded with a pair of sensors perpendicular to the valley axis. The spatially averaged coherency spectra on interstation separations are referred to as SPAC and are computed from the average of coherency spectra recorded from both arrays at each site.

Site DBL

The site DBL (detention basin of Launceston) was selected for its assumed location above the deepest part of the Tamar Valley (Fig. 1a). Sensors were positioned on footpaths of secondary roads with light traffic to reduce the statistical noise envelope on SPAC observations. Two 50-m-radius centered triangular arrays were used at site DBL. The first array was oriented with the pair of sensors XA_1 parallel to the valley axis ($\theta_1 = 315°$), and the second array was oriented with the pair of sensors XA_2 transverse to the valley axis ($\theta_2 = 45°$).

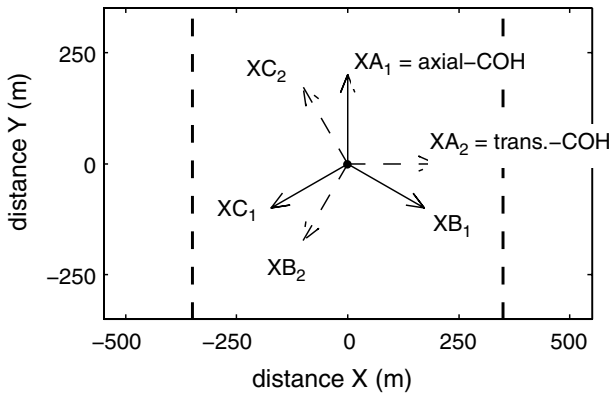

Figure 2. Orientation of two centered triangular arrays used in Launceston, with the pair of sensors XA_1 oriented parallel to the valley axis (axial-COH), and XA_2 perpendicular to the valley axis (transverse-COH). Thick dashed lines are the outlines of the valley.

The temporal stationarity in the microtremor wave field is increasingly important when using a limited number of sensors to record SPAC observations. The temporal stability of the microtremor wave field recorded at Launceston is improved by the removal of time segments presenting transient or abnormal behavior (Margaryan *et al.*, 2009). A total of $M_s = 15$ time segments were used for array 1, and $M_s = 21$ for array 2 at site DBL. Figure 3 presents the power spectra recorded at site DBL at sensors X and A from both arrays, for all time segments used in the interpretation and their time averaged power spectra.

The similarity of the power spectra on all time segments from each sensor, more obvious for $f \leq 2$ Hz, proves the temporal stability of microtremor propagation at site DBL; which was improved by the removal of transient time segments. The decrease in power spectra observed at approximately 1.0 Hz could be induced by a filtering effects of low-velocity sediments on vertical motion (Scherbaum *et al.*, 2003). This filtering effect is also observed on the HVSR curve, which shows a broad peak for 0.8 Hz $\leq f \leq$ 1.2 Hz).

The coherency spectra observed on all pairs of sensors and interstation separations of both arrays at site DBL are presented in Figure 4 on the frequency interval considered reliable to evaluate the SWV profile with SPAC at this site (0.75 Hz $\leq f \leq$ 11.5 Hz).

Visual analysis of the observed coherency spectra gives us some knowledge about the source distribution of the microtremor wave field. We observe little variability between the observed coherency spectra on pairs of sensors of different orientations for $f \leq 2.0$ Hz. This suggests the microtremor wave field has adequate azimuthal distribution to compute coherency spectra with pairs of sensors at these low frequencies. The increased variability of the observed coherency spectra with azimuth of the pair of sensors for $f >$ 2.0 Hz suggests the azimuthal averaging of observed coherency spectra is required to validate the spatial stationarity of the microtremor wave field at these higher frequencies. The source distribution at site DBL was studied in detail in Claprood and Asten (2010) by analyzing the variability of coherency spectra recorded on pairs of sensors oriented at different azimuths and comparing with SPAC on interstation separations. A frequency–wavenumber analysis conducted with the same two 50-m centered triangular arrays at site DBL (not presented) agrees well with the results determined by the observed coherency spectra at high frequencies. FK plots, however, have poor resolution to detect the direction of microtremor energy sources at frequencies lower than 1.6 Hz.

Site RGB

The rugby ground of Launceston (site RGB) is assumed to be located above the eastern flank of the Tamar Valley. SPAC observations at this site provide additional information about the soft sediments filling the Tamar Valley. This location was also chosen to test the SPAC method over a dipping bedrock interface. Two 50-m radius centered triangular arrays were laid out in the rugby ground, with the pair of sensors XA successively oriented parallel ($\theta_1 = 315°$) and perpendicular ($\theta_2 = 45°$) to the valley axis. SPAC observations were recorded with larger arrays at site RGB ($r_1 = 140$ m), but the high level of statistical noise restricts the analysis of coherency spectra recorded with these larger arrays. Figure 5 presents the power spectra recorded at site RGB on sensors X and A from both arrays.

The interpretation of SPAC observations is conducted on the frequency interval 0.5 Hz $\leq f \leq$ 4.25 Hz. The increase in power spectra at low frequency ($f \leq 0.5$ Hz) on array 2 is unexplained but does not impact the interpretation because it falls outside the valid frequency interval. The power spectra at some sensors (X_1, A_1) presents some variability at high frequencies, which suggest temporal nonstationarity of the microtremor wave field. The frequency interval upper limit was fixed at 4.25 Hz to validate the hypothesis of temporal stationarity of microtremors at site RGB. The azimuthal distribution of microtremor wave field is also verified at site RGB by analyzing the coherency spectra recorded on all pairs of sensors and interstation separations. The observed coherency spectra are presented in Figure 6.

The observed coherency spectra present some differences, depending on the azimuth of the pair of sensors they are computing. As previously analyzed in Claprood and Asten (2010), the microtremor wave field contains energy

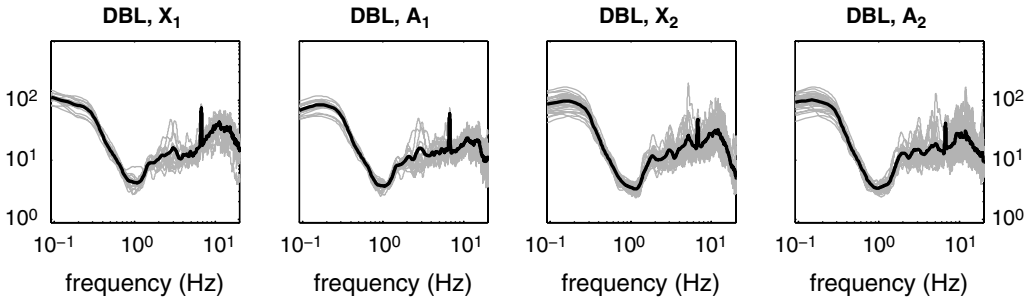

Figure 3. Power spectra recorded at site DBL. (Two left panels) Power spectra from array 1 at sensors X_1 and A_1 on $M_s = 15$ time segments. (Two right panels) Power spectra from array 2 at sensors X_2 and A_2 on $M_s = 21$ time segments. Gray lines, power spectra on each time segment; black lines, time averaged power spectra (logarithmic axis).

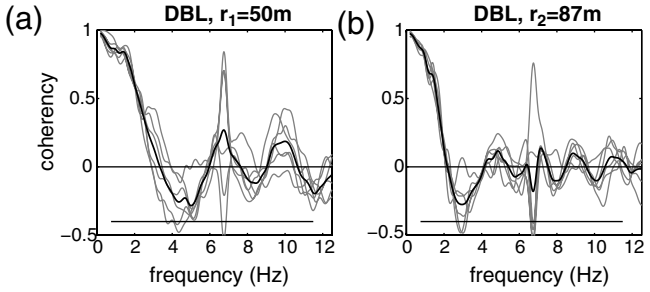

Figure 4. Observed coherency spectra at site DBL on all pairs of sensors and interstation separations of two centered triangular arrays for (a) $r_1 = 50$ m and (b) $r_2 = 87$ m. Gray lines, coherency spectra recorded on pairs of sensors; thick black lines, spatially averaged coherency spectra; solid line (at bottom of each graph), valid frequency interval at site DBL.

propagating from a restricted azimuth at site RGB for $f \geq 2.0$ Hz. The Tamar River and the busy Bathurst Street, located at approximately two array radii from the array center, are responsible for the restricted azimuth of the microtremor wave field. The variability of the observed coherency spectra is significantly reduced at lower frequency. The spatial averaging of coherency spectra on both interstation separations helps to significantly reduce the effect of the restricted azimuth distribution of the microtremor wave field at high frequency.

This analysis of the microtremor wave field was essential to better distinguish possible 2D effects from the valley and localized sources of microtremor. While the variability of the microtremor wave field at higher frequencies complicates the identification of 2D effects, it is suggested from the results of numerical simulations shown in the next section that 2D effects from the valley are occurring at frequencies lower than 2 Hz and could thus be identified on observed coherency spectra because the microtremor source distribution is more stable at these low frequencies.

We analyze the limit of resolution of the array geometry ($r_1 = 50$ m, $r_2 = 87$ m) deployed at both sites by computing the minimum frequency resolvable on both interstation separations following Henstridge (1979) criteria: $0.4 \leq rk$ and using equation (3):

$$f = \frac{0.4 V_{\max}(f)}{2\pi r}, \tag{5}$$

where $V_{\max}(f)$ is the maximum Rayleigh-wave velocity estimated at 880 m/s for the Tertiary sediments in-filling the valley (Michael-Leiba, 1995). Using equation (5), the minimum frequency resolvable at sites DBL and RGB is estimated at 1.12 Hz for interstation separation $r_1 = 50$ m and 0.64 Hz for $r_2 = 87$ m.

Numerical Simulations

Numerical simulations of microtremors in complex geological media are used to better control the parameters impacting the recording of coherency spectra in a 2D environment and to compare with coherency spectra observed at sites DBL and RGB in the Tamar Valley. The program package NOISE developed within the European Site Effects Assessment using Ambient Excitations (SESAME) project is used for the computation of seismic noise (microtremors) propagation in 3D heterogeneous geological structures with a planar free surface, from surface and near-surface random sources (Moczo and Kristek, 2002; J. Kristek, P. Moczo, and M. Kristekova, unpublished manuscript). The package is divided into two main programs: Ransource for the random space–time generation of microtremor point sources and Fdsim for the computation of seismic wave fields in 3D heterogeneous geological structures (Kristek *et al.*, 2002; Moczo *et al.*, 2002; Kristek *et al.*, 2009; Moczo *et al.*, 2007).

The source time functions were selected to be 50% deltalike signals (approximation to Dirac delta distribution), and 50% pseudomonochromatic functions of random duration and frequency. All source time functions were bandpass-filtered in the frequency range 0.4–3.0 Hz. The lower frequency boundary is selected to avoid the propagation of wavelengths larger than the size of the computational model. The upper frequency boundary is determined by the chosen grid spacing. A dense sampling of the shortest wavelengths of the wave field is required to avoid grid dispersion. A total of 79,442 point sources were space–time randomly distributed at the surface of a 9000 m × 3600 m grid over 100,000 time levels ($dt = 0.0014$ s), generating a 140-s

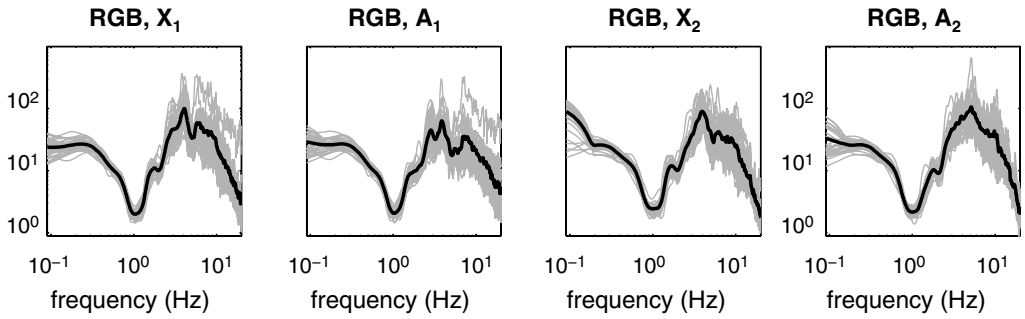

Figure 5. Power spectra recorded at site RGB. (Two left panels) Power spectra from array 1 at sensors X_1 and A_1 on $M_s = 38$ time segments. (Two right panels) Power spectra from array 2 at sensors X_2 and A_2 on $M_s = 32$ time segments. Same legend as for Figure 3.

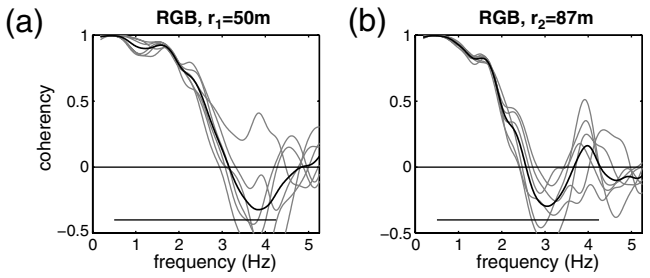

Figure 6. Observed coherency spectra at site RGB on all pairs of sensors and interstation separations of two centered triangular arrays for (a) $r_1 = 50$ m and (b) $r_2 = 87$ m. Same legend as for Figure 4.

time series. The locations of the point sources are presented in Figure 7.

We use a fine grid of $901 \times 361 \times 43$ cells and a coarse grid of $101 \times 41 \times 96$ cells to simulate the Tamar Valley, with a 10-m and 90-m spacing in the fine and coarse grids, respectively. Simulated SPAC arrays were positioned at two separate locations across the valley, with radii of 50 m and 100 m. The sensors are positioned to form centered triangular arrays with orientation XA_1 axial and XA_2 transverse to the valley axis to compare with SPAC observations recorded in Launceston. The location of all 26 receivers is plotted in Figure 8.

An analytical expression of the valley interface is input for the numerical simulations of surface waves. As suggested by the interpretation of gravity profiles from Leaman (1994), the valley geometry presents some asymmetry. The most appropriate function to represent the Tamar Valley with respect to horizontal distance x and depth z is the function

$$f(x,z) = \left(1+\frac{x}{a}\right)\left(1-\frac{x}{a}\right)^{\frac{1-\zeta}{1+\zeta}} - \left[(1+\zeta)(1-\zeta)^{\frac{1-\zeta}{1+\zeta}}\right]\frac{z}{H}, \tag{6}$$

where a is the valley half-width, H is the maximum depth, and ζ the asymmetry coefficient (Paolucci, 1999). Figure 9a shows the simulated Tamar Valley bedrock interface, with $a = 350$ m, $H = 250$ m, and $\zeta = -0.28571$. A layered

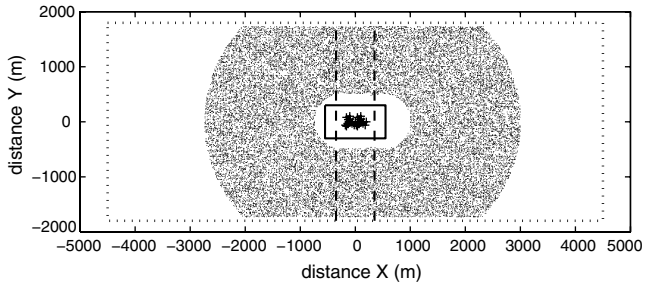

Figure 7. Simulated sources used in the numerical simulations of the Tamar Valley. Thick dotted line, the outline of the computational model; thick dashed vertical lines, edges of the simulated Tamar Valley; crosses, locations of receivers (represented in more detail in Figure 8).

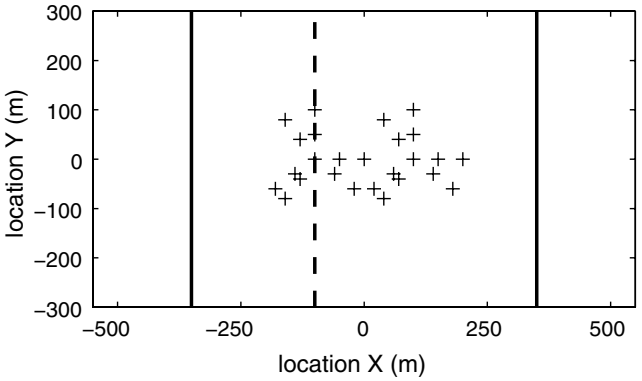

Figure 8. Location of simulated receivers across the model representation of the Tamar Valley. Arrays of radii 50 m and 100 m are presented for sites TamA($x = -100$ m) and TamB($x = 100$ m). Solid vertical lines, edges of the valley ($x = -350$ m, $x = 350$ m); dashed vertical line, the axis of the valley at its deepest point ($x = -100$ m).

earth with depth to bedrock $z = 25$ m at the right of the valley is interpreted from HVSR observations at Launceston (M. Claprood, M. Asten, and J. Kristek, unpublished manuscript).

Apart from lateral change in the bedrock interface, no lateral changes of velocity are considered in the overlaying sediments. This assumption was used to isolate and better understand the effect of a change in the bedrock interface and is justified by preliminary SPAC and FK results and SPAC observations recorded at 10 sites in Launceston (Claprood and Asten, 2009a, 2009b). The 1D SWV profile used in the simulations is presented in Figure 9b.

The 1D SWV profile presented in Figure 9b is an approximation of the SWV profile evaluated at site DBL from previous high-frequency coherency spectra analysis with constraints from a gravity survey and HVSR observations (Claprood and Asten, 2008a, 2008b).

The shallow Quaternary sediments are modeled as a 15-m layer of constant shear-wave velocity $V_S = 350$ m/s to suppress numerical instabilities at the free surface, where the steep sediment bedrock interface reaches the free surface

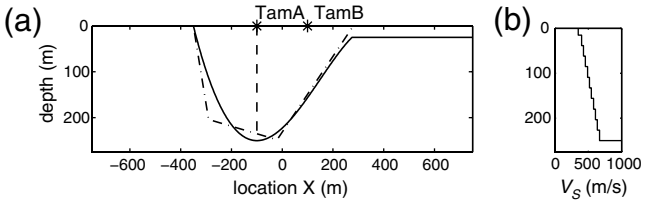

Figure 9. (a) Bedrock interface of model representation of Tamar Valley (vertical extension of 2). Sites TamA and TamB are the surface locations of the SPAC arrays' centers. Site TamA is located above the deepest point of the valley. Site TamB is located 200 m from site TamA. The bedrock interface at site TamB is 156 m deep, with a 38° slope. Dashed-dotted line is the geological interpretation of the bedrock interface from gravity profile 2 (Fig. 1b). Vertical dashed line in (a) is the location of SWV profile presented in (b), at the deepest point of the valley.

at the grid boundary in the perfectly matched layer zone. This approximation has negligible impact when analyzing the propagation of surface waves generated by the valley. We calculate a negligible difference of 0.02 Hz when evaluating the expected frequency of resonance computed with the observed SWV profile at site DBL and with the approximate SWV profile used in the simulations (thin 15-m layer with $V_S = 350$ m/s). This suggests the SWV profile used in the numerical simulations is an adequate approximation to represent the SWV evaluated in the Tamar Valley.

The shear-wave velocity of Tertiary sediments is represented by a linear function that varies from $V_S = 400$ m/s at depth $z = 15$ m to $V_S = 700$ m/s at depth $z = 250$ m. High quality factors were input for *S*-wave propagation ($1000 \leq Q_S \leq 2000$) and *P*-wave propagation ($1500 \leq Q_P \leq 8000$) to neglect the compressibility of sediments. This assumption is considered valid when dealing with low-amplitude waves such as microtremors.

Simulated SPAC

The outputs of the numerical simulations are the time series of the vertical and horizontal (X and Y components) ground velocity at all receivers. The vertical component time series of simulated microtremors are processed using the same steps used to process SPAC observations in Launceston. Figure 10 presents the power spectra simulated at the center sensors X and sensors A from two 50 m radius and two 100 m radius centered triangular arrays at site TamA.

The power spectra in Figure 10 show the restricted frequency interval input in the simulations. A rapid decrease in the energy level is observed at all sensors for $f > 3$ Hz, which corresponds to the higher frequency limit input as initial parameter. The simulated coherency spectra at different sites in the valley suggest the level of energy is sufficient to analyze SPAC curves for frequencies higher than 0.75 Hz. Sensors X and A_1 (from both 50-m and 100-m radius arrays) present almost identical power spectra. This was expected because all three sensors sample similar geology at the deepest point of the valley with a random source distribution. Small differences are observed between the power spectra of sensors A_2 when moving away from the deepest point of the valley at sensor X. The small increases in power spectra at approximately 1 Hz and 2 Hz are potentially induced by varying geology under the sensor.

The energy level drops rapidly at lower frequencies, which is partly explained by the lower frequency limit input in the simulations (0.4 Hz). We suggest the decrease in vertical microtremor energy at low frequency is further caused by the filtering effects of low-velocity sediments on vertical motion. A previous study (Claprood and Asten, 2008b) estimated the *SV* mode of resonance at 1.18 Hz on HVSR observations. Figure 11 presents the HVSR curves simulated at the center sensors X at sites TamA and TamB and observed at center sensors X at sites DBL and RGB.

HVSR simulated (site TamA) and observed (DBL) above the deepest point of the valley present similar features and shape, further suggesting that the 2D model of the valley is appropriate to represent the propagation of surface waves within the Tamar Valley.

Site TamA

The coherency spectra at site TamA, simulated from two 50-m radius centered triangular arrays above the deepest point of the model representation of the Tamar Valley, are presented in Figure 12. The pair of sensors XA_1 is oriented axially, and the pair of sensors XA_2 is transverse to the valley axis.

The results from two 100-m radius centered triangular arrays are presented in Figure 13 for improved resolution at low frequencies and to better detect the impact of the valley on simulated coherency spectra.

We observe from Figure 12 and Figure 13 that the simulated COH on all pairs of sensors present some variability for $f > 1.0$ Hz. Steplike features are observed on selected pairs of sensors at $f = 1.0$–1.5 Hz and $f = 2.0$–2.5 Hz. Such features associated with layered-earth sites have been interpreted as evidence for jumps to higher modes of propagation on the coherency spectrum (Asten *et al.*, 2004; Asten, 2006b). We suggest these shifts to higher modes of propagation on selected pairs of sensors are generated by 2D effects from the Tamar Valley.

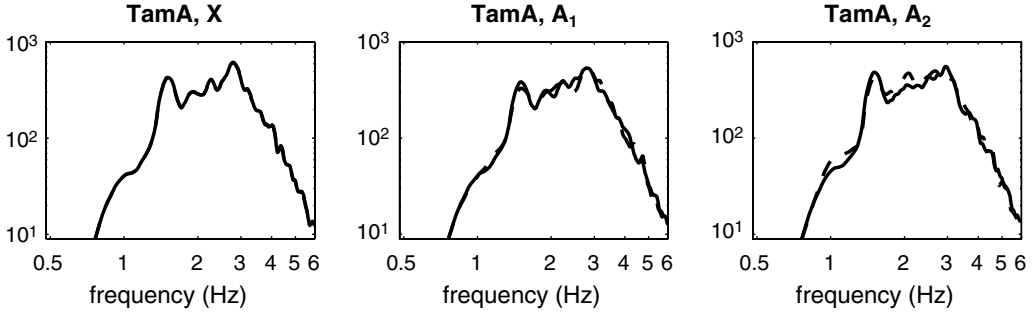

Figure 10. Simulated vertical power spectra at site TamA. (Left) Power spectra from sensor X. (Center) Power spectra from array 1 at sensor A_1. (Right) Power spectra from array 2 at sensor A_2. Nomenclature of sensors and geometry of arrays 1 and 2 are defined in Figure 2. Solid spectra are for 50-m radius triangular arrays, dashed spectra are for 100-m radius triangular arrays. Sensor X is the same for all arrays.

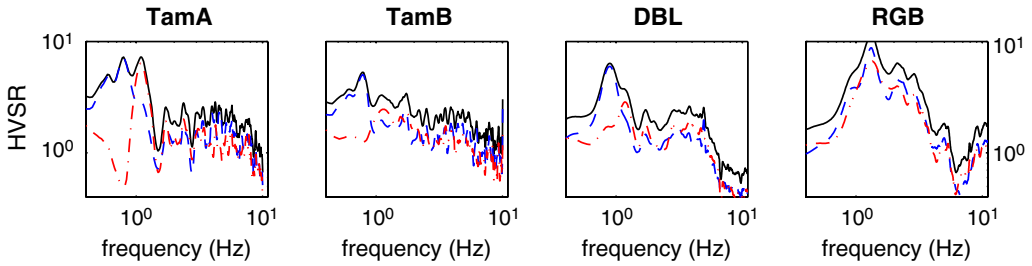

Figure 11. (Two left panels) Simulated HVSR at center sensors X at sites TamA and TamB. (Two right panels) Observed HVSR at center sensors X at sites DBL and RGB. Solid curves, total HVSR; dashed curves, axial component of HVSR; dashed-dotted curves, transverse component of HVSR. (X and Y axes are logarithmic). The color version of this figure is available only in the electronic edition.

We decompose the spatially averaged coherency spectra to analyze the behavior of simulated COH on selected pairs of sensors. The decomposition of COH into pairs of sensors at various azimuths was found to give indications on the source distribution of the microtremor wave field above a layered earth (Claprood and Asten, 2010). We postulate that similar methodology could assist in the detection of different modes of propagation in a valley environment, the valley polarizing the propagation of seismic surface waves. We present the simulated coherency spectrum at site TamA for pairs of sensors oriented parallel (axial-COH, pairs of sensors XA_1 and BC_2 from Figure 12 and Figure 13) and perpendicular (transverse-COH, pairs of sensors XA_2 and BC_1 from Figures 12 and 13) to the valley axis in Figure 14 and Figure 15. The theoretical coherency spectra of fundamental and first higher modes, computed from the SWV profile shown in Figure 9b for interstation separations $r_1 =$ 50–100 m and $r_2 =$ 80–160 m, are respectively drawn in dashed and dashed-dotted lines in Figure 14 and Figure 15.

We observe from Figure 14 and Figure 15 that the simulated axial-COH and transverse-COH show different patterns in the frequency interval 0.75–2 Hz. The jump to higher

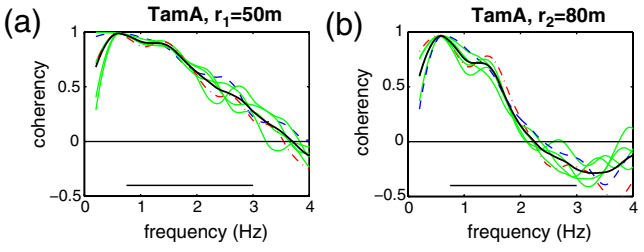

Figure 12. Simulated coherency spectrum (COH) at site TamA on all pairs of sensors and interstation separations of two centered triangular arrays for (a) $r_1 = 50$ m and (b) $r_2 = 80$ m. Thick solid lines are spatially averaged coherency spectra (SPAC) on interstation separations. Dashed lines are coherency spectra on pairs of sensors parallel to the valley axis: XA_1 on (a) and BC_2 on (b). Dashed-dotted lines are coherency spectra on pairs of sensors transverse to the valley axis: XA_2 on (a) and BC_1 on (b). Thin solid lines are coherency spectra on all other pairs of sensors of the array. Pairs of sensors are named following the nomenclature presented in Figure 2. Straight line at bottom of each graph presents frequency interval where theoretical COH is fit to simulated COH. The color version of this figure is available only in the electronic edition.

modes of propagation, already observed in Figure 12 and Figure 13, is better defined on simulated transverse-COH at $f = 1.0$ Hz $- 1.5$ Hz and is of increasing amplitude with increasing interstation separation. This jump is not present on simulated axial-COH, which more closely follows the theoretical COH. The simulated transverse-COH presents the highest level of roughened imaginary coherency spectrum in the frequency interval 1.0 Hz $\leq f \leq$ 2.0 Hz (black bars on Fig. 14 and Fig. 15). This high statistical noise seems to be azimuth dependent and is not observed on axial-COH and SPAC. The presence of high values of roughened imaginary coherency spectra could be induced by high-frequency numerical instabilities generated by boundary effects of the finite size grid used in the numerical simulations.

We summarize the MSR values computed between the theoretical COH and simulated axial-COH, transverse-COH, and SPAC at site TamA on the frequency interval 0.75 Hz $\leq f \leq$ 3.0 Hz for the $r_1 = 50$ m array and 0.75 Hz $\leq f \leq$ 2.5 Hz for the $r_1 = 100$ m array in Table 1. Different frequency intervals were selected to compare theoretical and simulated COH in function on the array size in order to restrict the analysis of coherency spectra computed with single pairs of sensors up the first minimum of the Bessel function, as suggested by Okada (2006) and Claprood and Asten (2010).

Lower values of the MSR on most axial-COH ($r = 80$ m, 100 m, or 160 m), when compared to transverse-COH and SPAC on the selected frequency interval, suggest the use of axial-COH alone is preferable to evaluate the 1D SWV profile from the microtremor time series simulated

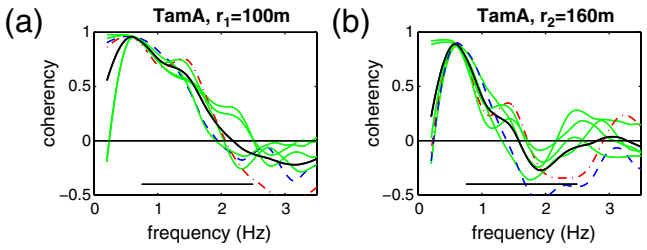

Figure 13. Simulated COH at site TamA on all pairs of sensors and interstation separations of two centered triangular arrays for (a) $r_1 = 100$ m and (b) $r_2 = 160$ m. Same legend as for Figure 12. The color version of this figure is available only in the electronic edition.

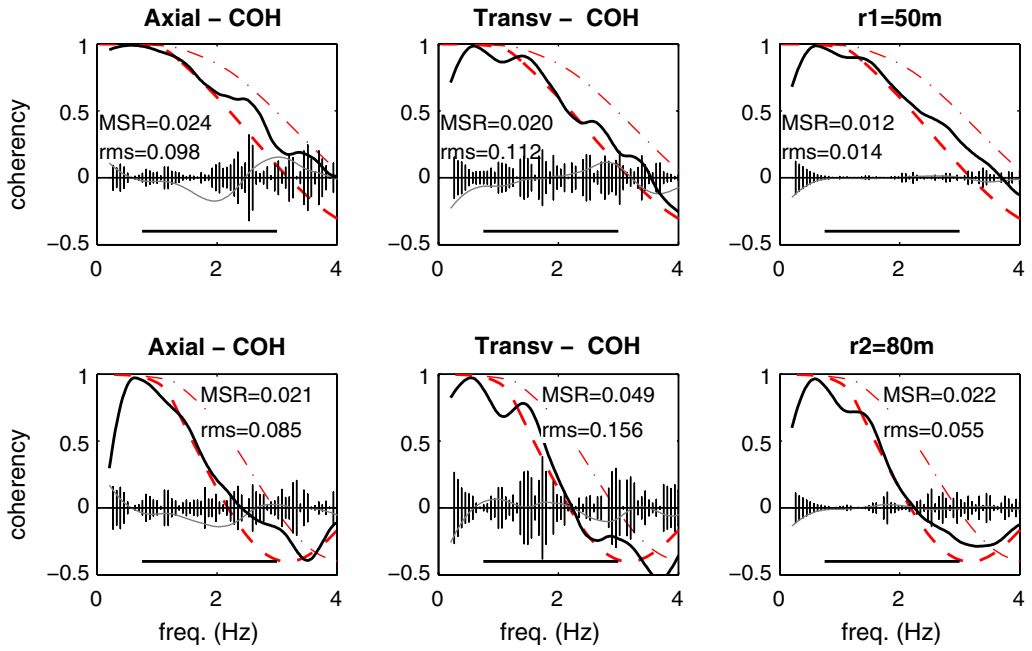

Figure 14. Best-fit coherency models for pairs of sensors and interstation separations (top row) $r_1 = 50$ m and (bottom row) $r_2 = 80$ m at site TamA. SPAC (right column) were computed from all pairs of sensors ($n = 6$) from two centered triangular arrays. Thick solid black curve, real component of simulated COH; gray solid curve, smoothed imaginary component of simulated COH; bars, roughened imaginary component of simulated COH; dashed curve is theoretical COH, fundamental mode for preferred layered-earth model; dashed-dotted curve, theoretical COH, first higher mode. The straight line at the bottom of each graph presents the frequency interval where theoretical COH is fit to simulated COH. MSR, mean square of residuals; rms_{Im}, root mean square of the roughened imaginary component. The color version of this figure is available only in the electronic edition.

above the deepest point of a valley. It is an indication that the simulated axial-COH presents the highest degree of similarity to the theoretical COH when considering the fundamental mode of propagation of Rayleigh waves.

As suggested in Claprood and Asten (2010), we compute MSR factors to evaluate the azimuth dependency and the impact of spatial averaging of simulated coherency spectra at site TamA. The MSR factors are computed as the ratio

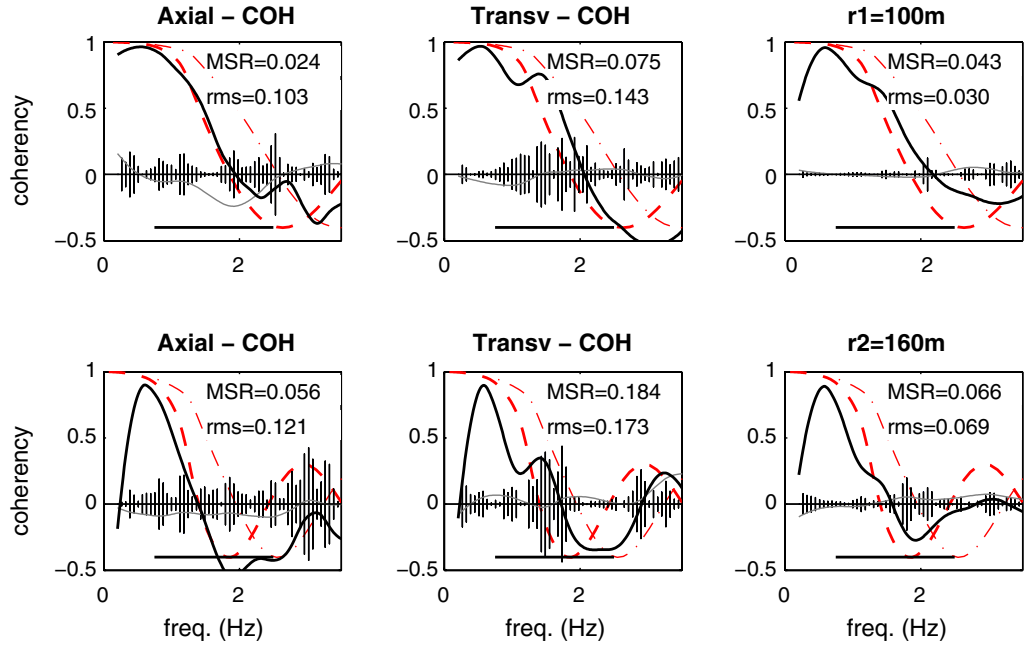

Figure 15. Best-fit coherency models for pairs of sensors and interstation separations (top) $r_1 = 100$ m and (bottom) $r_2 = 160$ m at site TamA. Same legend as for Figure 14. The color version of this figure is available only in the electronic edition.

Table 1
Mean Square of Residuals (MSR) between Simulated and Theoretical COH at Site TamA

r	MSR ax-COH*	MSR tr-COH*	MSR SPAC
$r_1 = 50$ m	0.024	0.020	0.012
$r_2 = 80$ m	0.021	0.049	0.022
$r_1 = 100$ m	0.024	0.075	0.043
$r_2 = 160$ m	0.056	0.184	0.066

*ax, axial; tr, transverse.

of MSR values in two different situations. For example, we compute an MSR factor of 0.6 between the simulated axial-COH and SPAC for $r = 100$ m at site TamA by dividing the MSR on axial-COH (0.024 from Table 1) by the MSR on SPAC (0.43 from Table 1). An MSR factor of 0.6 indicates the MSR computed on simulated axial-COH is smaller than the MSR computed on SPAC with $r = 100$ m at site TamA. This suggests that the axial-COH provides a better fit to the theoretical coherency spectra to evaluate the 1D SWV profile. We use MSR factors to compare coherency spectra simulated (or observed) on pairs of sensors of different azimuths and spatially averaged coherency spectra.

Table 2 presents MSR factors computed at site TamA. The MSR factor referred to as ax-COH/SPAC is the ratio between the MSR on axial-COH and the MSR on SPAC. The MSR factor referred to as tr-COH/SPAC is the ratio between the MSR on transverse-COH and the MSR on SPAC, while the MSR factor referred to as tr-COH/ax-COH is the ratio between the MSR on transverse-COH and the MSR on axial-COH.

The results from Table 2 further indicate that axial-COH is the preferred option to evaluate a 1D SWV profile above the deepest point of the valley at site TamA for the selected frequency interval. The MSR factors ax-COH/SPAC are lower or equal to $1.0x$ for all interstation separations except $r = 50$ m. In Figure 14 (top left panel), the simulated axial-COH closely follows the theoretical COH for $r = 50$ m, and departure from the theoretical COH is observed for frequencies greater than 2 Hz.

Site TamB

Simulated coherency spectra are recorded at site TamB, modeling a location over the sloping flank of the Tamar Valley. We present the simulated COH for pairs of sensors oriented parallel (axial-COH) and perpendicular (transverse-COH) to the valley axis in Figure 16 and Figure 17.

We observe that the simulated coherency spectra present a different pattern at site TamB compared to site TamA. The jump to a higher mode of propagation is not observed on pairs of sensors at $f = 1.0$ Hz–1.5 Hz at site TamB. Higher MSR on axial-COH and transverse-COH in comparison with SPAC on larger interstation separations, which are more sensitive to deeper material, suggest the conventional azimuthal averaging of coherency spectra is preferable in evaluating the 1D SWV profile down to the basement at site TamB. Localized high values of statistical noise (high rms_{lm}) is also observed at most pairs of sensors on the simulated coherency spectra.

MSR computed for axial-COH, transverse-COH, and SPAC are summarized in Table 3. As completed for site TamA, we present the MSR factors computed at site TamB in Table 4.

High MSR factors on both axial-COH and transverse-COH relative to SPAC for most interstation separations further strengthen the evidence that the azimuthal averaging of coherency spectra is needed to evaluate the 1D SWV profile at site TamB for the selected frequency interval. The high MSR factors computed from axial-COH to SPAC at site TamB for larger interstation separations, compared to those evaluated at site TamA (Table 2), is evidence that the varying geological conditions impact the two locations differently.

The analysis of the coherency spectra simulated at sites TamA and TamB in the model representation of the Tamar Valley suggests the decomposition of the spatially averaged coherency spectrum into components oriented parallel (axial-COH) and perpendicular (transverse-COH) to the valley axis is an effective method for the recognition of 2D effects induced by the deep and narrow Tamar Valley. This effect is seen as a jump to higher modes of propagation at $f = 1.0$ Hz–1.5 Hz on the transverse-COH at site TamA, located above the deepest point of the model representation of the valley. Possible 2D effects could be detected at higher frequency (jump to higher modes at $f = 2.0$ Hz–2.5 Hz at site TamA) but would be difficult to isolate on observed coherency spectra at sites DBL and RGB due to the increased variability of the observed coherency spectra at higher frequency.

The results from the numerical simulations suggest that the coherency spectra computed on pairs of sensors oriented parallel to the valley axis (axial-COH) can provide a reliable estimation of 1D SWV structure above the deepest point of a valley because its fit to the theoretical coherency spectrum presents lower MSR than the transverse-COH or the spatially averaged coherency spectrum.

Table 2
Mean Square of Residuals Factors (MSR Fx) at Site TamA

r	MSR Fx (ax-COH/SPAC)*	MSR Fx (tr-COH/SPAC)*	MSR Fx (tr-COH)/(ax-COH)*
$r_1 = 50$ m	2.0	1.7	0.8
$r_2 = 80$ m	1.0	2.2	2.3
$r_1 = 100$ m	0.6	1.7	3.1
$r_2 = 160$ m	0.9	2.8	3.3

*ax, axial; tr, transverse.

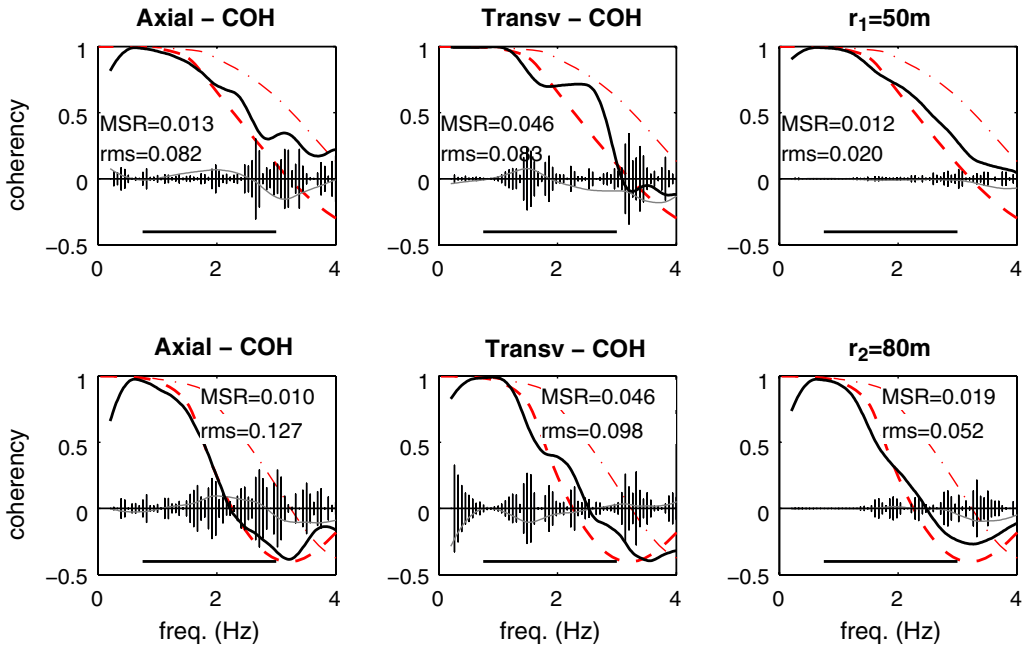

Figure 16. Best-fit coherency models from pairs of sensors and interstation separations (top) $r_1 = 50$ m and (bottom) $r_2 = 80$ m at site TamB. Same legend as for Figure 14. The color version of this figure is available only in the electronic edition.

Observed SPAC

Similar methodology was applied at sites DBL and RGB in Launceston to validate the results obtained from the numerical simulations and to detect the effects of rapid changes in geology across the Tamar Valley. Site DBL is assumed to be located above the deepest point of the Tamar Valley in order to compare with site TamA, and site RGB is located in the east flank of the valley at similar position to that of site TamB.

Site DBL

Coherency spectra were recorded at site DBL with two 50-m-radius centered triangular arrays. The heavy traffic on Wellington Street and the steep hill on Frankland Street west

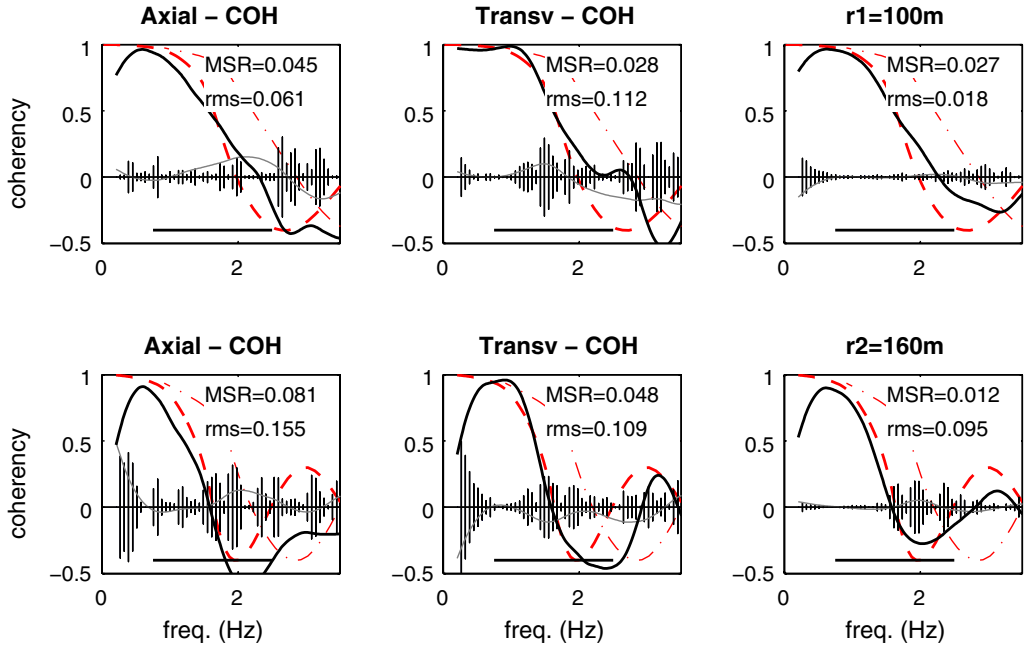

Figure 17. Best-fit coherency models from pairs of sensors and interstation separations (top) $r_1 = 100$ m and (bottom) $r_2 = 160$ m at site TamB. Same legend as for Figure 14. The color version of this figure is available only in the electronic edition.

Table 3
Mean Square of Residuals (MSR) between Simulated and Theoretical COH at Site TamB

r	MSR ax-COH*	MSR tr-COH*	MSR SPAC*
$r_1 = 50$ m	0.013	0.046	0.012
$r_2 = 80$ m	0.010	0.046	0.019
$r_1 = 100$ m	0.045	0.028	0.027
$r_2 = 160$ m	0.081	0.048	0.012

*ax, axial; tr, transverse.

of the DBL array (Fig. 1) were the principal constraints in deploying arrays of larger aperture at this site.

We apply the methodology followed on simulated coherency spectra to extract (from Fig. 4) the coherency spectra recorded with pairs of sensors parallel and perpendicular to the valley axis on the frequency interval 0.75 Hz $\leq f \leq$ 3.0 Hz. The fit between observed axial-COH, transverse-COH, and SPAC to theoretical COH is presented in Figure 18.

Axial-COH and SPAC agree well with the theoretical COH computed from the preferred SWV profile at site DBL, for both interstation separations $r_1 = 50$ m and $r_2 = 87$ m. Transverse-COH presents the worst fit to the theoretical COH, on which a steplike feature similar to that observed on simulated transverse-COH at site TamA is recognized at $f = 1.0$–1.5 Hz. This feature, not seen on axial-COH, is postulated to represent a jump to a higher mode of propagation.

A drop in coherency, interpreted as a filtering effect from the low-velocity sediments, is observed at frequencies less than 1.0 Hz on most pairs of sensors. This is an indication of a low level of energy on the vertical component of microtremors at frequencies approximately equal to and lower than the expected frequency of resonance, also shown on the HVSR curves in Figure 11. Both axial-COH and transverse-COH show approximately the same level of statistical noise. No frequency-dependent pattern, such as the pattern observed on simulated roughened imaginary coherency spectrum at site TamA, are recognized on the observed roughened imaginary coherency spectra at site DBL.

The distribution of MSR with the azimuth of the pair of sensors and the spatial averaging of coherency spectra is analyzed at site DBL by computing MSR factors such as those evaluated on the simulated coherency spectra. The results from the MSR factors analysis at site DBL are presented in Table 5. The reader is referred to Table 2 for comparison with MSR factors computed on the simulated coherency spectra at site TamA above the deepest point of the model representation of the Tamar Valley.

Lower values of MSR factors computed from axial-COH to SPAC (ax-COH/SPAC), in comparison to those computed from transverse-COH (tr-COH/SPAC), support the interpretation that coherency spectra observed on pairs of sensors oriented parallel to the valley axis are the preferred option to evaluate the SWV profile above the deepest point of the Tamar Valley. MSR factors computed at site DBL for $r_2 = 87$ m present similar values to those computed on the simulated coherency spectra at site TamA for $r_2 = 80$ m (Table 2).

The preferred 1D SWV profile at site DBL is interpreted from the observed coherency spectra recorded in Launceston. The shallowest layers were previously interpreted with a 20-m-radius centered hexagonal array during the 2006 field survey for 1.5 Hz $\leq f \leq$ 23 Hz (Claprood and Asten, 2008a) and with the spatial averaging of coherency spectra of the 50-m-radius centered triangular arrays for 3.0 Hz $\leq f \leq$ 11.5 Hz (Claprood and Asten, 2010). Interpretation of SPAC observations agrees well with shallow borehole logs (maximum depth of 20 m) held by the Launceston City Council.

Interpretation of coherency spectra simulated (site TamA) and observed (site DBL) above the deepest point of the Tamar Valley suggests that the axial-COH provides the best fit to the theoretical coherency spectrum at low frequency, corresponding to deeper sediments. The depth to bedrock interface at site DBL is thus constrained by fitting the observed coherency spectra recorded on pairs of sensors oriented parallel to the valley axis (axial-COH, Fig. 18, left panels) to the theoretical COH for 0.75 Hz $\leq f \leq$ 3.0 Hz. The preferred 1D SWV profile interpreted at site DBL is presented in Figure 19a.

We complete a sensitivity study to confirm that the interface of the Tamar Valley at depth $z = 250$ m can be detected by the 50-m-radius centered triangular arrays used at site DBL with interstation separations $r_1 = 50$ m and $r_2 = 87$ m. We follow the methodology from Arai and Tokimatsu (2004), varying the thickness of the deepest layer by a value equivalent to $\pm 10\%$ and $\pm 20\%$ of the total thickness of sediments from the preferred SWV profile, and we analyze the changes on the theoretical coherency spectra computed from the alternative SWV profiles thus generated. The sensitivity D_{ij} from a change in total thickness of sediment H is expressed as

Table 4
Mean Square of Residuals Factors (MSR Fx) at Site TamB

r	MSR Fx (ax-COH/SPAC)*	MSR Fx (tr-COH/SPAC)*	MSR Fx (tr-COH)/(ax-COH)*
$r_1 = 50$ m	1.1	3.9	3.6
$r_2 = 80$ m	0.5	2.4	4.7
$r_1 = 100$ m	1.7	1.0	0.6
$r_2 = 160$ m	6.8	4.0	0.6

*ax, axial; tr, transverse.

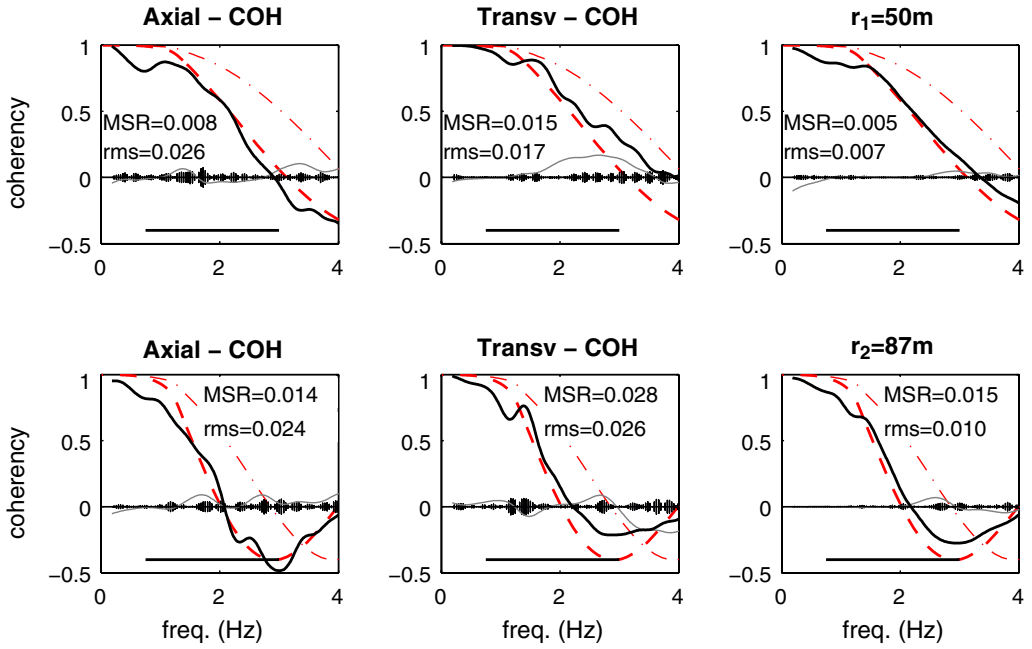

Figure 18. Best-fit coherency models from pairs of sensors and interstation separations (top) $r_1 = 50$ m and (bottom) $r_2 = 87$ m at site DBL. Same legend as for Figure 14. The color version of this figure is available only in the electronic edition.

$$D_i^H(f) = \left| \frac{H}{J_0(f)} \times \frac{\partial J_0(f)}{\partial H} \right|_{H=H_i}, \tag{7}$$

where J_0 is the theoretical coherency spectrum, and i corresponds to the change in the parameter evaluated ($H \pm 10\%$ and $H \pm 20\%$). The results from the sensitivity study are presented in Figure 19b.

While the absolute values of sensitivity are not high, the variation of sensitivity (most significant on interstation separation r_2, Fig. 19b) at 1.0 Hz $\leq f \leq$ 2.0 Hz, with a change in total thickness of 10% or 20%, confirms the capabilities of observed COH at site DBL to locate the bedrock interface at depth $z = 250$ m. The frequency for which the jump to a higher mode of propagation was detected on transverse-COH (Fig. 18) is included in this frequency interval. It further strengthens the idea that the differences observed in the behavior of axial-COH and transverse-COH can be induced by the sensitivity of each component to the different modes of propagation that develop in the Tamar Valley. The infinite peak observed at $f \simeq 2.0$ Hz on r_2 (Fig. 19b, right panel) is induced by the zero crossing of the Bessel function at that frequency and is a mathematical artifact of equation (7).

We evaluate the MSR between the observed coherency spectra on axial-COH, transverse-COH, and SPAC and from the theoretical COH computed from the preferred and alternative SWV profiles obtained from the sensitivity study. We also evaluate MSR factors between the MSR computed on alternative SWV profiles and the MSR computed on the preferred SWV profile on axial-COH, transverse-COH, and SPAC. Table 6 presents a summary of MSR and MSR factors computed during the sensitivity study at site DBL.

While the variations in MSR are quite small, clear tendencies can be observed from Table 6. As expected, the interstation separation r_2 is more sensitive to a change in the total thickness of sediments. While the MSR computed on SPAC stay constant with a variation in thickness, MSR values on axial-COH and transverse-COH have opposite reactions. Shallowing the bedrock interface ($H - 20\%$, $H - 10\%$) worsens the fit obtained with axial-COH, while it improves the fit obtained with transverse-COH. Deepening the interface ($H + 20\%$, $H + 10\%$) seems to improve the fit obtained with axial-COH, while it has no effect on the fit obtained with transverse-COH. We suggest the lower MSR on axial-COH with a deeper bedrock interface is an artifact induced by

Table 5
Mean Square of Residuals Factors (MSR Fx) at Site DBL

r	MSR Fx (ax-COH/SPAC)*	MSR Fx (tr-COH/SPAC)*	MSR Fx (tr-COH)/(ax-COH)*
$r_1 = 50$ m	1.6	3.0	1.9
$r_2 = 87$ m	0.9	1.9	2.0

*ax, axial; tr, transverse.

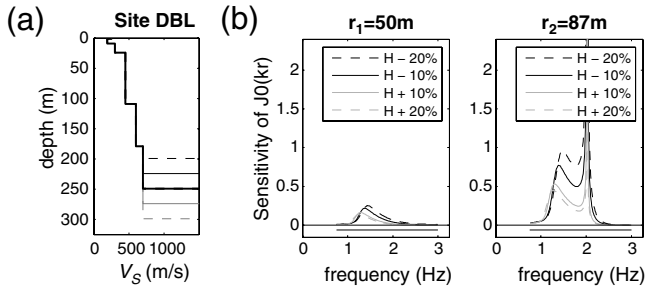

Figure 19. (a) Preferred 1D SWV profile interpreted at site DBL (thick black line). Thin gray and black lines are alternative SWV profiles used in the sensitivity study. (b) Sensitivity study on theoretical COH by varying the total sediment thickness by $H \pm 10\%$ and $H \pm 20\%$. Straight line at bottom of graph presents the valid frequency interval at site DBL.

the observed drop in coherency spectra for frequencies lower than the frequency of resonance. The opposite reaction to a change in sediments thickness observed on axial-COH and transverse-COH further supports the idea that the two components record different information from the microtremor wave field propagating in the Tamar Valley.

Site RGB

Coherency spectra were recorded at site RGB with two 50-m-radius centered triangular arrays. Figure 20 shows the observed coherency spectra at site RGB, recorded with pairs of sensors parallel (axial-COH) and perpendicular (transverse-COH) to the valley axis and the spatially averaged coherency spectra for interstation separations $r_1 = 50$ m and $r_2 = 87$ m.

Observed coherency spectra at site RGB are interpreted for 0.5 Hz $\leq f \leq$ 4.25 Hz. All observed coherency spectra (axial-COH, transverse-COH, SPAC) agree well with the theoretical COH computed from the preferred SWV profile at site RGB. Observed COHs from all azimuths present a drop in coherency at approximately 1.0 Hz, effects which might be induced by the filtering effects of low-velocity sediments at the frequency of resonance, evaluated at $f = 1.31$ Hz from HVSR (Fig. 11).

A jump to a higher mode of propagation is observed on transverse-COH at $f \geq 2.0$ Hz, while it is only lightly detectable on r_2 on axial-COH. The decomposition of SPAC into pairs of sensors, presented in Claprood and Asten (2010), has suggested the presence of limited azimuth distribution of microtremor energy at site RGB, which might mask possible 2D effects induced by the Tamar Valley at these frequencies. We suggest this jump to higher mode, associated with highly cyclic behavior of the smoothed imaginary coherency spectrum (gray curve, Fig. 20) is induced by limited azimuth sampling in the microtremor wave field.

An MSR analysis similar to that conducted at site DBL is presented in Table 7 to better analyze the azimuth sampling of observed coherency spectra at site RGB.

High MSR factors between the MSR computed on axial-COH and transverse-COH with respect to SPAC suggest the importance of spatial averaging the observed coherency spectra at site RGB to obtain a reliable evaluation of the 1D SWV profile. MSR factors ax-COH/SPAC and tr-COH/SPAC present similar values for both interstation separations. This further strengthens the hypothesis that neither axial-COH nor tranverse-COH should be used alone to evaluate the 1D SWV profile at site RGB. This is a significant difference when compared with site DBL, where the axial-COH was the preferred option to evaluate the SWV profile.

This difference is explained by the location of both sites within the valley; site RGB is located above the gentle slope on the eastern flank of the Tamar Valley, which can be estimated as a layered earth, while site DBL is assumed to be located above the deepest point of the Tamar Valley, where a 2D resonance is expected to develop. The HVSR curves presented in Figure 11 also suggest that the approximation of a 1D layered earth is valid at site RGB, where both axial and transverse components of HVSR show a peak at the same frequency.

Similar to completed at site DBL, a sensitivity study was completed to analyze the possibility of detecting the bedrock

Table 6
Mean Square of Residuals and MSR Factors* between Axial-COH, Transverse-COH, and SPAC Recorded at Site DBL and Theoretical COH Computed from Preferred and Alternative SWV Profiles

	ax-COH† $r_1 = 50$ m	tr-COH† $r_1 = 50$ m	SPAC $r_1 = 50$ m	ax-COH† $r_2 = 87$ m	tr-COH† $r_2 = 87$ m	SPAC $r_2 = 87$ m
MSR Computed from Preferred SWV Profile						
H‡	0.008	0.015	0.005	0.014	0.028	0.015
MSR (and MSR Factors*) Computed from Alternative SWV Profiles						
$H - 20\%$‡	0.009(1.1x)	0.014(0.9x)	0.005(1.0x)	0.018(1.3x)	0.025(0.9x)	0.015(1.0x)
$H - 10\%$‡	0.008(1.0x)	0.015(1.0x)	0.005(1.0x)	0.015(1.1x)	0.027(1.0x)	0.015(1.0x)
$H + 10\%$‡	0.007(0.8x)	0.015(1.0x)	0.005(1.0x)	0.012(0.9x)	0.028(1.0x)	0.015(1.0x)
$H + 20\%$‡	0.007(0.9x)	0.015(1.0x)	0.004(0.8x)	0.011(0.8x)	0.028(1.0x)	0.014(0.9x)

*MSR factors (in parentheses) are computed as the ratio of MSR from alternative SWV profiles to MSR from preferred SWV profile.

†ax, axial; tr, transverse.

‡H, total thickness of sediment.

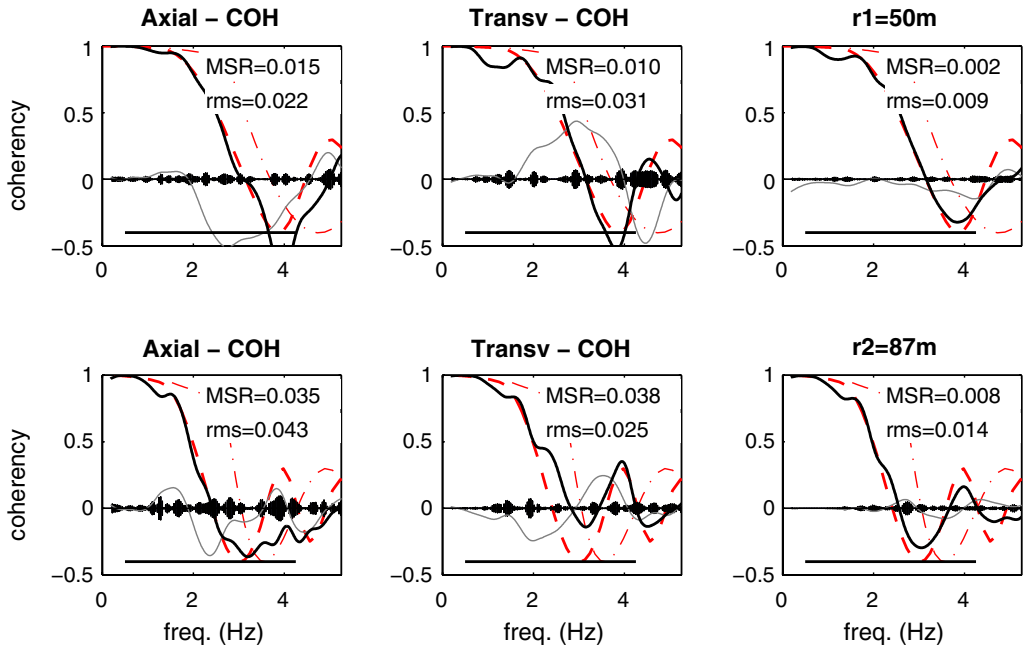

Figure 20. Best-fit coherency models from pairs of sensors and interstation separations (top) $r_1 = 50$ m and (bottom) $r_2 = 87$ m at site RGB. Same legend as for Figure 14. The color version of this figure is available only in the electronic edition.

interface on the valid frequency interval used at site RGB. The results are presented in Figure 21.

The sensitivity study shows that there is little sensitivity to changes in the bedrock interface at site RGB; this is true even if the depth to bedrock interface is interpreted as much shallower than at site DBL. We believe the shallow sediments of very low velocity that were encountered at site RGB have a masking effect, limiting the resolution at greater depth.

Residuals Analysis

An analysis of residuals between the simulated and observed coherency spectra from all interstation separations of all arrays and the theoretical coherency spectra J_0 computed from the preferred 1D SWV helps us to summarize the results obtained at Launceston. Figure 22 presents the frequency distribution of residuals computed at simulated sites TamA and TamB and observed sites DBL and RGB. The residuals are computed as the difference between each component of the simulated or observed coherency spectra (axial-COH, transverse-COH, SPAC) and the theoretical coherency spectrum on the valid frequency interval.

Figure 22 better represents the differences between all components of simulated or observed coherency spectra and the theoretical coherency spectra (Bessel function J_0). The residuals computed from the transverse-COH (dashed-dotted curves, Fig. 22a–d) show a peak-and-trough feature at $f = 1.0$–1.5 Hz at site TamA. The amplitude of the peaks and the troughs on transverse-COH residuals is increasing with larger interstation separation. This feature is not observed on axial-COH (dashed curves, Fig. 22a–d). The residuals computed from SPAC present a behavior between those of axial-COH and transverse-COH. No such trend can be observed at site TamB (Fig. 22e–h), where the residuals behave more randomly regardless of the component from which they are computed.

The peak and trough feature on the residuals of transverse-COH is also observed at site DBL, for $r = 87$ m, while it is not present on the other components (axial-COH and SPAC in Fig. 22i,j). Residuals at site RGB behave in a similar way, regardless of the component used to compute them (Fig. 22k,l). At all simulated and observed arrays, we clearly observe more variability in the residuals for higher frequencies ($f \geq 2.0$ Hz) for axial-COH and transverse-COH,

Table 7
Mean Square of Residuals Factors (MSR Fx) at Site RGB

r	MSR Fx (ax-COH/SPAC)*	MSR Fx (tr-COH/SPAC)*	MSR Fx (tr-COH)/(ax-COH)*
$r_1 = 50$ m	7.5	5.0	0.7
$r_2 = 87$ m	4.4	4.8	1.1

*ax, axial; tr, transverse.

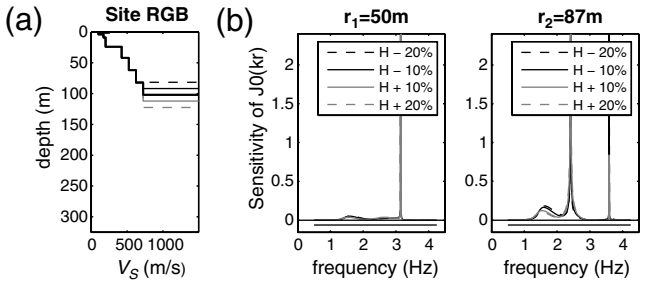

Figure 21. (a) Preferred 1D SWV profile interpreted at site RGB (thick black line). Thin gray and black lines are alternative SWV profiles used in the sensitivity study. (b) Sensitivity study on theoretical COH by varying the total sediment thickness by $H \pm 10\%$ and $H \pm 20\%$. Straight line at bottom of graph presents the valid frequency interval at site RGB.

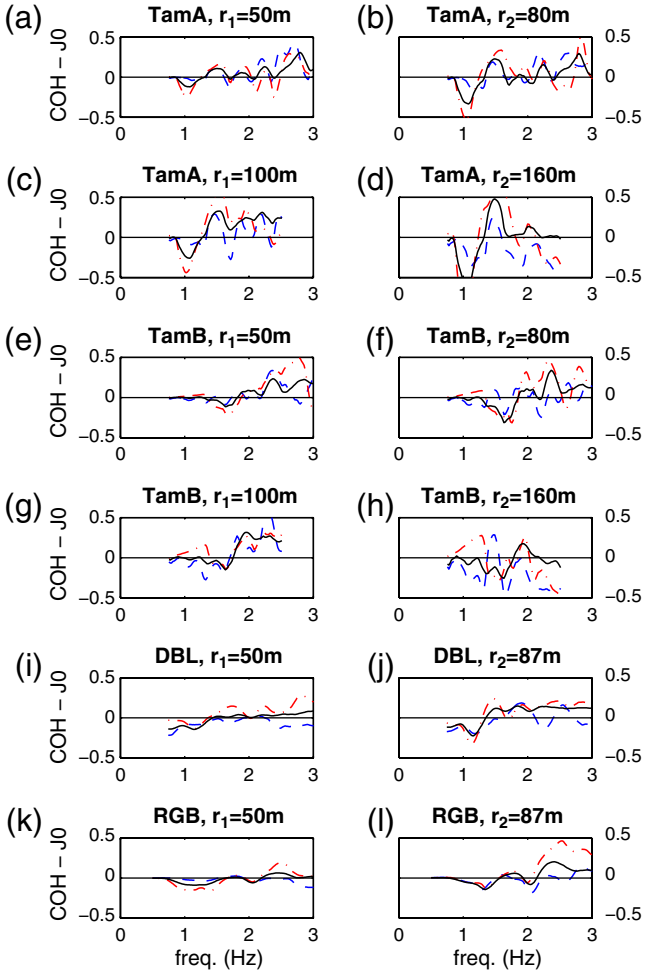

Figure 22. Distribution of residuals with frequency for all interstation separations at simulated arrays (a,b,c,d) TamA and (e,f,g,h) TamB and at observed arrays (i,j) DBL and (k,l) RGB. Solid curves, simulated or observed SPAC minus theoretical Bessel function J_0; dashed curves, simulated or observed axial-COH minus J_0; dashed-dotted curves, simulated or observed transverse-COH minus J_0. The color version of this figure is available only in the electronic edition.

while the residuals computed from SPAC show more stability.

1D SWV Profiles

The preferred SWV profiles interpreted at sites DBL and RGB are presented in Figure 23a. Figure 23b shows the shear-wave slowness profiles to better represent the variations in velocity in the low-velocity layers, as suggested by Boore and Asten (2008).

Significant differences are observed between the preferred SWV profiles interpreted at sites DBL and RGB. The shallow layers ($z < 25$ m) at site RGB have significantly lower velocity (greater slowness; Fig. 23b) than the shallow sediments at site DBL. This could be explained by the proximity of the site RGB to the Tamar River (Fig. 1a), where the shallow sediments are known to possess very little cohesion, thus lower shear-wave velocity. Sediments with velocity varying between 400 m/s and 700 m/s are interpreted as sands and clays from the Tertiary period, filling most of the Tamar Valley. Tertiary sediments are significantly thicker at site DBL; the interface with the Jurassic dolerite bedrock is interpreted at approximately $z = 250$ m at site DBL and $z = 100$ m at site RGB. Because of the poor sensitivity of the arrays at site RGB, the bedrock interface at this location is best constrained by HVSR observations (J. Kristek, P. Moczo, and M. Kristekova, unpublished manuscript).

Interpretation of Results

As described in Bard and Bouchon (1985), and later identified by Steimen *et al.* (2003), Frischknecht and Wagner (2004), Roten *et al.* (2006), and Lenti *et al.* (2009), different modes of resonance develop in a valley environment. In shallow valleys, Bard and Bouchon's model states that surface waves are generated from the edges of the valley and propagate back and forth within the sediments, inducing a 1D pattern of resonance. In deep and narrow valleys, different modes of resonance develop (*SH*, *SV*, *P*), with their

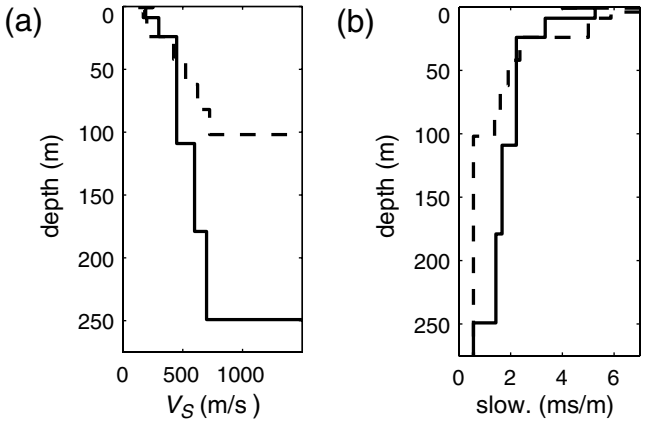

Figure 23. Preferred (a) 1D SWV-to-depth profiles and (b) 1D slowness-to-depth profiles at sites DBL (solid lines) and RGB (dashed lines).

own frequencies of resonance and components of motion. The Bard and Bouchon (1985) model states that a 2D pattern of resonance develops in valleys with a shape ratio (referred to as the ratio of maximum depth H to width at half-depth w) greater than a critical shape ratio. The model recognizes the development of a 2D pattern of resonance by the generation of standing waves from the bottom of the valley and indicates that edge-generated surface waves can also be detected.

As evaluated in Claprood and Asten (2008b), a 2D *SV* frequency of resonance is identified in the Tamar Valley (shape ratio of 0.59) at $f = 1.18$ Hz at site DBL. The shape ratio is computed as the ratio of the maximum sediments thickness ($H = 250$ m) to the width at half-depth ($w = 421$ m) evaluated from the model representation of the valley (Fig. 9a). The velocity contrast is computed for a dolerite bedrock shear-wave velocity estimated at 1800 m/s and sediment shear-wave velocity of 350–700 m/s, evaluated from the SWV profile used in the simulations at the deepest point of the valley at site TamA (Fig. 9b).

The Bard and Bouchon (1985) model indicates that the excitation of *SV* waves induces mostly Rayleigh waves of first higher mode of propagation in shallow valleys. Rayleigh waves of first higher mode have a greater velocity, which approximately equals the *P*-wave velocity of sediments at the frequency of resonance of a layered earth. These edge-generated waves propagate from one edge of the valley to the other in a direction perpendicular to the valley axis.

We suggest the observed coherency spectra recorded by the pairs of sensors oriented transverse to the valley axis can detect the transverse motion of propagation of these edge-generated waves. This is suggested by the jump to higher mode of propagation recognized on simulated (site TamA) and observed (site DBL) transverse-COH recorded above the deepest point of the valley; this jump occurs at a frequency approximately equal to the *SV* frequency of resonance of the Tamar Valley.

From the absence of a jump on the axial-COH curves, we suggest the axial-COH is free of the higher mode of surface wave propagation at $f = f^{SV}_{\text{fund}}$ and can be used with reliability to evaluate a 1D SWV profile in valley environment, as demonstrated by numerical simulations and SPAC observations in the Tamar Valley.

Conclusion

Numerical simulations of the propagation of seismic waves from ambient seismic sources (microtremors) in a valley environment and microtremor observations in the Tamar Valley in Launceston (Tasmania, Australia) were used to assess the potential usefulness of the SPAC method in studying complex geology. The recording of coherency spectra on pairs of sensors oriented parallel (axial-COH) and perpendicular (transverse-COH) to the valley axis optimizes the capability of the SPAC method to detect the existence of the valley, to identify its *SV* mode of resonance, and, most importantly, to evaluate a 1D SWV profile above the deepest point of the valley. The use of axial-COH alone is recommended only when microtremor sources are recorded for sufficient long time and are distributed over a wide range of azimuth, both assumptions being necessary for a meaningful SPAC estimate using single pair of sensors.

We observe that coherency spectra recorded above the deepest point of the valley with pairs of sensors oriented perpendicular to the valley axis can detect high-velocity edge-generated surface waves at the *SV* frequency of resonance. This was recognized on simulated transverse-COH at site TamA and on observed transverse-COH at site DBL above the deepest point of the Tamar Valley, as a jump to faster velocity on coherency spectra at a frequency approaching the *SV* fundamental frequency of resonance.

We suggest that the coherency spectra of the vertical component computed on pairs of sensors oriented parallel to the valley axis (axial-COH) is not affected by the propagation of these edge-generated waves of higher velocity. No jump to higher mode of propagation was detected on simulated or observed axial-COH, which closely follows the theoretical coherency spectra computed from the preferred SWV profile.

Lower mean square of residuals between simulated and theoretical coherency spectra on axial-COH, when compared to MSR values on transverse-COH and SPAC, suggest that the coherency spectra recorded on pairs of sensors oriented parallel to the valley axis are the preferred option to evaluate a 1D SWV profile above the deepest point of the valley.

This is observed on simulated coherency spectra at site TamA from 50-m-radius and 100-m-radius centered triangular arrays. Observed coherency spectra recorded at site DBL above the deepest point of the valley suggest similar conclusions. MSR values computed between observed axial-COH at site DBL and theoretical coherency spectra are lower or approximately equal to MSR values computed for SPAC and are significantly lower than MSR values computed on transverse-COH. This suggests that the observed coherency spectra recorded with pairs of sensors parallel to a valley axis provide a reliable evaluation of the 1D SWV profile at sites located above the deepest point of a deep and narrow valley, such as demonstrated above the Tamar Valley in Launceston.

Simulated coherency spectra in the sloping flank of the valley (site TamB) suggest that no effect of the higher velocity propagating surface waves is observed at this location. We suggest the gently dipping interface of this side of the valley dissipates the propagation of edge-generated higher mode waves. Numerical simulations suggest it is preferable to use the spatially averaged coherency spectrum to evaluate the 1D SWV profile at site TamB, at which site the assumption of a layered earth holds true for microtremor studies. The coherency spectra observed at site RGB in the flank of the Tamar Valley prorogate the interpretation completed on simulated coherency spectra at site TamB. The presence of 1D and 2D modes of resonance within the same valley has also been observed by Lenti *et al.* (2009).

These initial results demonstrate the capability of SPAC observations to detect the existence of a 2D structure, and to interpret 1D SWV profiles in the environment of a deep and narrow valley such as the Tamar Valley with a shape ratio of 0.59. SPAC observations are combined with HVSR microtremor observations recorded in Launceston to complete the site resonance study of the Tamar Valley (J. Kristek, P. Moczo, and M. Kristekova, unpublished manuscript). Additional field observations with larger arrays would help gain resolution at depth, although at this site the deployment of larger arrays was restricted by the street layout. The use of three-component SPAC observations should provide additional information, in particular by permitting the detection of the *SH* mode of resonance, which develops in valley environments.

Data and Resources

All data used in this paper came from published sources listed in the references. Information on the geology of Launceston is available from unpublished maps from Mineral Resources Tasmania, borehole logs held by Launceston City Council, and a gravity survey completed by Leaman (1994).

Acknowledgments

Maxime Claprood is supported by a Monash Graduate Scholarship, an International Postgraduate Research Scholarship, and a Québec's Funds for Nature and Technology Scholarship. Seismometers used in this project were loaned to Monash University by the Australian National Seismic Imaging Resource (ANSIR). We are grateful to the City Council of Launceston for their assistance during field surveys. Geological maps of Launceston were provided by Mineral Resources Tasmania. We would like to recognize the help of Janett Steiner for her assistance during the field survey. We wish to thank associate editor Stefano Parolai and two anonymous reviewers, whose comments helped improve the manuscript.

References

Aki, K. (1957). Space and time spectra of stationary stochastic waves, with special reference to microtremors, *Bull. Earthq. Res. Inst.* **35,** 415–456.

Arai, H., and K. Tokimatsu (2004). *S*-wave velocity profiling by inversion of microtremor H/V spectrum, *Bull. Seismol. Soc. Am.* **94,** no. 1, 53–63.

Asten, M. (1976). *The Use of Microseisms in Geophysical Exploration*, *Ph.D. Thesis*, Macquarie University, Sydney, Australia.

Asten, M. (2003). Lessons from alternative array design used for high-frequency microtremor array studies, paper no. 14, in *Earthquake Risk Mitigation*, J. Wilson, N. Lam, G. Gibson, and B. Butler (Editors), Australian Earthquake Engineering Society, Melbourne, Australia, 7 pp.

Asten, M. (2005). An assessment of information on the shear-velocity profile at Coyote Creek, San Jose, from SPAC processing of microtremor array data, in *Blind Comparisons of Shear-Wave Velocities at Closely Spaced Sites in San Jose, California* M. Asten and D. Boore (Editors), *U.S. Geol. Surv. Open-File Rept. 2005-1169*, available online at http://pubs.usgs.gov/of/2005/1169/.

Asten, M. (2006a). On bias and noise in passive seismic data from finite circular array data processed using SPAC methods, *Geophysics* **71,** no. 6, V153–V162, doi 10.1190/1.2345054.

Asten, M. (2006b). Site shear velocity profile interpretation from microtremor array data by direct fitting of SPAC curves, paper no. 99 in *Proc. of the 3rd International. Symp. on the Effects of Surface Geology on Seismic Motion*, vol. 2, P.-Y. Bard, E. Chaljub, C. Cornou, F. Cotton, and P. Guéguen (Editors), LCPC Editions, Grenoble, France, 1069–1080.

Asten, M., T. Dhu, and N. Lam (2004). Optimised array design for microtremor array studies applied to site classification; comparison of results with SCPT logs, paper no. 2903, in *Proc. of the 13th World Conf. on Earthquake Engineering* Vancouver, Canada, 1–6 August 2004

Asten, M., N. Lam, G. Gibson, and J. Wilson (2002). Microtremor survey design optimised for application to site amplification and resonance modelling, paper no. 7, in *Total Risk Management in the Privatised Era*, M. Griffith, D. Love, P. McBean, A. McDougall, and B. Butler (Editors), Australian Earthquake Engineering Society, Adelaide, Australia, 7 pp.

Bard, P.-Y., and M. Bouchon (1985). The two-dimensional resonance of sediment-filled valleys, *Bull. Seismol. Soc. Am.* **75,** no. 2, 519–541.

Bettig, B., P.-Y. Bard, F. Scherbaum, J. Riepl, F. Cotton, C. Cornou, and D. Hatzfeld (2001). Analysis of dense array noise measurements using the modified spatial auto-correlation method (SPAC). Application to the Grenoble area, *Boll. Geof. Teor. Appl.* **42,** 281–304.

Bonnefoy-Claudet, S., F. Cotton, and P.-Y. Bard (2006). The nature of noise wavefield and its applications for site effects studies. A literature review, *Earth Sci. Rev.* **79,** 205–227, available online at www.sciencedirect.com.

Boore, D., and M. Asten (2008). Comparisons of shear-wave slowness in the Santa Clara Valley, California, using blind interpretations of data from invasive and noninvasive methods, *Bull. Seismol. Soc. Am.* **98,** no. 4, 1983–2003, doi 10.1785/0120070277.

Capon, J. (1969). High-resolution frequency-wavenumber spectrum analysis, *Proc. IEEE* **57,** no. 8, 1408–1418.

Capon, J. (1973). Signal processing and frequency-wavenumber spectrum analysis for a large aperture seismic array, in *Methods in Computational Physics*, vol. **13,** Academics Press Inc., New York, 1–59.

Chávez-García, F., and M. Rogríguez (2007). The correlation of microtremors: Empirical limits and relations between results in frequency and time domains, *Geophys. J. Int.* **171,** 657–664, doi 10.1111/j.1365-246X.2007.03529.x.

Chávez-García, F., T. Domínguez, M. Rodríguez, and F. Pérez (2007). Site effects in a volcanic environment: A comparison between HVSR and array techniques at Colima, Mexico, *Bull. Seismol. Soc. Am.* **97,** no. 2, 591–604, doi 10.1785/0120060095.

Chávez-García, F., M. Rodríguez, and W. Stephenson (2005). An alternative approach to the SPAC analysis of microtremors: Exploiting stationarity of noise, *Bull. Seismol. Soc. Am.* **95,** no. 1, 277–293, doi 10.1785/0120030179.

Cho, I., T. Tada, and Y. Shinozaki (2004). A new method to determine phase velocities of Rayleigh waves from microseisms, *Geophysics* **69,** no. 6, 1535–1551, doi 10.1190/1.1836827.

Cho, I., T. Tada, and Y. Shinozaki (2006a). A generic formulation for microtremor exploration methods using three-component records from a circular array, *Geophys. J. Int.* **165,** 236–258, doi 10.1111/j.1365-246X.2006.02880.

Cho, I., T. Tada, and Y. Shinozaki (2006b). Centerless circular array method: Inferring phase velocities of Rayleigh waves in broad wavelength ranges using microtremor records, *J. Geophys. Res.* **111,** B09315, 12 pp., doi 10.1029/2005JB004235.

Cho, I., T. Tada, and Y. Shinozaki (2008). Assessing the applicability of the spatial autocorrelation method: A theoretical approach, *J. Geophys. Res.* **113,** B06307, doi 10.1029/2007JB005245.

Claprood, M., and M. Asten (2008a). Comparison of array microtremor survey methods for estimation of dispersion curves in Launceston, Australia, in *Symposium on the Application of Geophysics to Engineering and Environmental Problems (SAGEEP)*, Environmental and Engineering Geophysical Society, Philadelphia, Pennsylvania, 8 pp.

Claprood, M., and M. Asten (2008b). Microtremor survey methods in the Tamar Valley, Launceston, Tasmania: Evidence of 2D resonance from

microtremor observations, paper no. 20, in *Proceedings of the Earthquake Engineering in Australia 2008 Conference*, N. Lam, J. Wilson, G. Gibson, and S. Anderson (Editors), Australian Earthquake Engineering Society, Ballarat, Australia, 8 pp.

Claprood, M., and M. Asten (2009a). Initial results from spatially averaged coherency, frequency-wavenumber, and horizontal to vertical spectrum ratio microtremor survey methods for site hazard study at Launceston, Tasmania, *Explor. Geophys.*, **40,** no. 1, 132–142, doi 10.1071/EG08106.

Claprood, M., and M. Asten (2009b). Variability of shear wave velocity structures in Launceston, Tasmania, in *Proceedings of the Earthquake Engineering in Australia 2009* Australian Earthquake Engineering Society, Newcastle, Australia, 11–13 December 2009.

Claprood, M., and M. Asten (2010). Statistical validity control on SPAC microtremor observations recorded with a restricted number of sensors, *Bull. Seismol. Soc. Am.* **100,** no. 2, 776–791, doi 10.1785/0120090133.

Cornou, C., P.-Y. Bard, and M. Dietrich (2003a). Contribution of dense array analysis to the identification and quantification of basin-edge-induced waves, Part I: Methodology, *Bull. Seismol. Soc. Am.* **93,** no. 6, 2604–2623.

Cornou, C., P.-Y. Bard, and M. Dietrich (2003b). Contribution of dense array analysis to the identification and quantification of basin-edge-induced waves, Part II: Application to Grenoble basin (French Alps), *Bull. Seismol. Soc. Am.* **93,** no. 6, 2624–2648.

Ekström, G., G. Abers, and S. Webb (2009). Determination of surface-wave phase velocities across USArray from noise and Aki's spectral formulation, *Geophys. Res. Lett.* **36,** L18301, doi 10.1029/2009GL039131.

Fäh, D., G. Stamm, and H.-B. Havenith (2007). Analysis of three-component ambient vibration array measurements, *Geophys. J. Int.* 1–15, doi 10.1111/j.1365-246X.2007.03625.x.

Field, E. (1996). Spectral amplification in a sediment-filled valley exhibiting clear basin-edge-induced waves, *Bull. Seismol. Soc. Am.* **86,** no. 4, 991–1005.

Frischknecht, C., and J.-J. Wagner (2004). Seismic soil effect in an embanked deep alpine valley: A numerical investigation of two-dimensional resonance, *Bull. Seismol. Soc. Am.* **94,** no. 1, 171–186.

García-Jerez, A., F. Luzón, and M. Navarro (2008). An alternative method for calculation of Rayleigh and Love wave phase velocities by using three-component records on a single circular array without a central station, *Geophys. J. Int.* **173,** 844–858, doi 10.1111/j.1365-246X.2008.03756.x.

Goldstein, P., and R. Archuleta (1987). Array analysis of seismic signals, *Geophys. Res. Lett.* **14,** no. 1, 13–16.

Hartzell, S., D. Carver, R. Williams, S. Harmsen, and A. Zerva (2003). Site response, shallow shear-wave velocity, and wave propagation at the San Jose, California, dense seismic array, *Bull. Seismol. Soc. Am.* **93,** no. 1, 443–464.

Hartzell, S., D. Carver, T. Seiji, K. Kudo, and R. Herrmann (2005). Shallow shear-wave velocity measurements in the Santa Clara Valley; Comparison of spatial autocorrelation (SPAC) and frequency wavenumber (FK) methods, in *Blind comparison of shear-wave velocities at closely spaced sites in San Jose, California*, M. Asten and D. Boore (Editors), *U.S. Geol. Surv., Open-File Rept. 2005-1169*, 5 pp., available online at http://pubs.usgs.gov/of/2005/1169,

Henstridge, J. (1979). A signal processing method for circular arrays, *Geophysics* **44,** no. 2, 179–184.

Herrmann, R. (2002). *Computer Programs in Seismology: An Overview of Synthetic Seismogram Computation*, version 3.30, Saint Louis University, St. Louis, Missouri.

Horike, M. (1985). Inversion of phase velocity of long-period microtremors to the *S*-wave velocity structure down to the basement in urbanized areas, *J. Phys. Earth* **33,** 59–96.

Köhler, A., M. Ohrnberger, F. Scherbaum, M. Wathelet, and C. Cornou (2007). Assessing the reliability of the modified three-component spatial autocorrelation technique, *Geophys. J. Int.* **168,** 779–796, doi 10.1111/j.1365-246X.2006.03253.x.

Kristek, J., P. Moczo, and R. Archuleta (2002). Efficient methods to simulate planar free surface in the 3D 4th-order staggered grid finite-difference schemes, *Studia Geophys. Geod.* **46,** 355–381.

Kristek, J., P. Moczo, and P. Pazak (2009). Numerical modeling of earthquake motion in Grenoble basin, France, using a 4th-order velocity-stress arbitrary discontinuous staggered-grid FD scheme, in *Proc. of the 3rd International. Symp. on the Effects of Surface Geology on Seismic Motion*, vol. **2**, P.-Y. Bard, E. Chaljub, C. Cornou, F. Cotton, and P. Guéguen (Editors), LCPC Editions, Grenoble, France, ISSN 1628-4704, 1517–1526.

Kudo, K., T. Kanno, H. Okada, O. Özel, M. Erdik, T. Sasatani, S. Higashi, M. Takahashi, and K. Yoshida (2002). Site-specific issues for strong ground motions during the Kocaeli, Turkey, earthquake of 17 August 1999, as inferred from array observations of microtremors and aftershocks, *Bull. Seismol. Soc. Am.* **92,** no. 1, 448–465.

Lacoss, R., E. Kelly, and M. Toksöz (1969). Estimation of seismic noise structure using arrays, *Geophysics* **34,** no. 1, 21–38.

Leaman, D. (1994). Assessment of gravity survey City of Launceston, *Tech. Rept., Leaman Geophysics, Hobart, Tasmania, Australia, for Launceston City Corporation Seismic Zonation Study*, 10 pp.

Lenti, L., S. Martino, A. Paciello, and G. Scarascia Mugnozza (2009). Evidence of two-dimensional amplification effects in an alluvial valley (Valnerina, Italy) from velocimetric records and numerical models, *Bull. Seismol. Soc. Am.* **99,** no. 3, 1612–1635, doi 10.1785/0120080219.

Margaryan, S., T. Yokoi, and K. Hayashi (2009). Experiments on the stability of the spatial autocorrelation method (SPAC) and linear array methods and on the imaginary part of the SPAC coefficients as an indicator of data quality, *Explor. Geophys.* **40,** no. 1, 121–131, doi 10.1071/EG08101.

Michael-Leiba, M. (1995). Microtremor survey and seismic microzonation Launceston, Tasmania, *Tech. Rept., Australian Geological Survey, Canberra, ACT, Australia, for Launceston City Council*, 14 pp.

Moczo, P., and J. Kristek (2002). FD code to generate noise synthetic, *SESAME Tech. Rept. D02.09, European Commission: Research General Directorate*, Project No. EVG1-CT-2000-00026, available online at http://sesame-fp5.obs.ujf-grenoble.fr, 31 pp.

Moczo, P., J. Kristek, V. Vavryčuk, R. Archuleta, and L. Halada (2002). 3D heterogeneous staggered-grid finite-difference modeling of seismic motion with volume harmonic and arithmetic averaging of elastic moduli and densities, *Bull. Seismol. Soc. Am.* **92,** no. 8, 3042–3066.

Moczo, P., J. Robertsson, and L. Eisner (2007). The finite-difference time-domain method for modeling of seismic wave propagation, *Adv. Geophys.* **48,** 421–516, doi 10.1016/S0065-2687(06)48008-0.

Morikawa, H., S. Sawada, and J. Akamatsu (2004). A method to estimate phase velocities of Rayleigh waves using microseisms simultaneously observed at two sites, *Bull. Seismol. Soc. Am.* **94,** no. 3, 961–976.

Ohori, M., A. Nobata, and K. Wakamatsu (2002). A comparison of ESAC and FK methods of estimating phase velocity using arbitrarily shaped microtremor arrays, *Bull. Seismol. Soc. Am.* **92,** no. 6, 2323–2332.

Okada, H. (2003). *The Microtremor Survey Method*, Geophysical Monograph Series, no. 12, Fitterman, D. V. (Series Editor) and Asten, M. W. (Volume Editor)Society of Exploration Geophysicists, Tulsa, Oklahoma, 135 pp.

Okada, H. (2006). Theory of efficient array observations of microtremors with special reference to the SPAC method, *Explor. Geophys.* **37,** no. 1, 73–85.

Paolucci, R. (1999). Shear resonance frequencies of alluvial valleys by Rayleigh's method, *Earthq. Spectra* **15,** no. 3, 503–521.

Picozzi, M., S. Parolai, D. Bindi, and A. Strollo (2009). Characterization of shallow geology by high-frequency seismic noise tomography, *Geophys. J. Int.* **176,** 164–174, doi 10.1111/j.1365-246X.2008.03966.x.

Roberts, J., and M. Asten (2005). Estimating the shear velocity profile of Quaternary silts using microtremor array (SPAC) measurements, *Explor. Geophys.* **36,** 34–40.

Roten, D., and D. Fäh (2007). A combined inversion of Rayleigh wave dispersion and 2-D resonance frequencies, *Geophys. J. Int.* **168,** 1261–1275, doi 10.1111/j.1365-246X.2006.03260.x.

Roten, D., D. Fäh, C. Cornou, and D. Giardini (2006). Two-dimensional resonances in Alpine valleys identified from ambient vibration wavefields, *Geophys. J. Int.* **165,** 889–905.

Roten, D., D. Fäh, K. Olsen, and D. Giardini (2008). A comparison of observed and simulated site response in the Rhône valley, *Geophys. J. Int.* **173,** 958–978, doi 10.1111/j.1365-246X.2008.03774.x.

Scherbaum, F., K.-G. Hinzen, and M. Ohrnberger (2003). Determination of shallow shear wave velocity profiles in the Cologne, Germany area using ambient vibrations, *Geophys. J. Int.* **152,** 597–612.

Schmidt, R. (1986). Multiple emitter location and signal parameter estimation, *IEEE Trans. Antenn. Propag.* **AP-34,** no. 3, 276–280.

Steimen, S., D. Fäh, F. Kind, C. Schmid, and D. Giardini (2003). Identifying 2D resonance in microtremor wave fields, *Bull. Seismol. Soc. Am.* **93,** no. 2, 583–599.

Stephenson, W., S. Hartzell, A. Frankel, M. Asten, D. Carver, and W. Kim (2009). Site characterization for urban seismic hazards in lower Manhattan, New York City, from microtremor array analysis, *Geophys. Res. Lett.* **36,** L03301, doi 10.1029/2008GL036444.

Tokimatsu, K. (1997). Geotechnical site characterization using surface waves, in *Earthquake Geotechnical Engineering: Proceedings IS-Tokyo 95, the first International. Conf. on Earthq. Geotech. Eng.*, K. Ishihara (Editor), A. A. Balkema, Rotterdam, The Netherlands, 1333–1368

Tokimatsu, K., S. Tamura, and H. Kojima (1992). Effects of multiple modes on Rayleigh wave dispersion characteristics, *J. Geotech. Eng.* **118,** no. 10, 1529–1543.

Toksöz, M. (1964). Microseisms and an attempted application to exploration, *Geophysics* **29,** no. 2, 154–177.

Toksöz, M., and R. Lacoss (1968). Microseisms: Mode structure and sources, *Science* **159,** 872–873.

Udías, A. (1999). *Principles of Seismology* Cambridge University Press, Cambridge, United Kingdom, 475 pp.

Uebayashi, H. (2003). Extrapolation of irregular subsurface structures using the horizontal-to-vertical spectral ratio of long-period microtremors, *Bull. Seismol. Soc. Am.* **93,** no. 2, 570–582.

Wathelet, M., D. Jongmans, M. Ohrnberger, and S. Bonnefoy-Claudet (2008). Array performances for ambient vibrations on a shallow structure and consequences over *Vs* inversion, *J. Seismol.* **12,** 1–19, doi 10.1007/s10950-007-9067-x.

School of Geosciences
Monash University
Melbourne, Victoria 3800, Australia
Maxime.Claprood@ete.inrs.ca
Michael.Asten@sci.monash.edu.au
(M.C., M.W.A.)

Faculty of Mathematics, Physics and Informatics
Comenius University, Bratislava
Mlynska dolina F1
842 48 Bratislava, Slovak Republic
Jozef.Kristek@fmph.uniba.sk
(J.K.)

Manuscript received 27 August 2009